

SUBSPACE METHOD OF MOMENTS FOR *AB INITIO* 3-D SINGLE-PARTICLE CRYO-EM RECONSTRUCTION

JEREMY HOSKINS, YUEHAW KHOO, OSCAR MICKELIN, AMIT SINGER, AND YUGUAN WANG

ABSTRACT. Cryo-electron microscopy (Cryo-EM) is a widely-used technique for recovering the 3-D structure of biological molecules from a large number of experimentally generated noisy 2-D tomographic projection images of the 3-D structure, taken from unknown viewing angles. Through computationally intensive algorithms, these observed images are processed to reconstruct the 3-D structures. Many popular computational methods rely on estimating the unknown angles as part of the reconstruction process, which becomes particularly challenging at low signal-to-noise ratio. The method of moments (MoM) offers an alternative approach that circumvents the estimation of viewing angles of individual projection images by instead estimating the underlying distribution of the viewing angles, and is robust to noise given sufficiently many images. However, the method of moments typically entails computing high-order moments of the projection images, incurring significant storage and computational costs.

To mitigate this, we propose a new approach called the subspace method of moments (subspace MoM), which compresses the first three moments using data-driven low-rank tensor techniques as well as expansion into a suitable function basis. The compressed moments can be efficiently computed from the set of projection images using numerical quadrature and can be employed to jointly recover the 3-D structure and the distribution of viewing angles. We illustrate the practical applicability of the subspace MoM in numerical experiments using up to the third-order moment, which significantly improves the resolution of MoM reconstructions compared to previous approaches.

1. INTRODUCTION

Cryo-EM [60] is a powerful imaging technique that enables the study of biological molecules, including proteins and nucleic acids, at near-atomic resolution. This technique involves freezing many copies of a given molecule in a thin layer of ice. The sample is then imaged using an electron microscope. The resulting projection image, termed a *micrograph*, consists of many two-dimensional projections of the three-dimensional molecule. Due to thermal motion, the copies of the molecules in the sample rotate before freezing. The projections in the micrograph therefore consist of tomographic projections of randomly rotated copies of the molecule. A *particle picking* procedure [10, 35] is then employed to extract the individual projections from the micrograph. An example of a micrograph and the result of particle picking are shown in Figure 1. Once extracted, the goal of Cryo-EM is to recover the three-dimensional structure of the molecule from the projection images. A significant impediment to the practical application of Cryo-EM is the large amount of noise present in the images. This noise, arising due to radiation damage of the sample, can easily obscure critical features, making accurate reconstruction difficult.

One popular method for Cryo-EM reconstruction is based on maximum likelihood estimation [62, 26], using Expectation Maximization (EM) typically referred to as 3-D iterative refinement [57]. This method refines a 3-D model using the 2-D projections until it closely matches experimental data. The EM approach has been extremely successful in determining high resolution structures of large macromolecules. However, EM fails to produce meaningful reconstruction for molecules whose molecular weight is below ~ 40 kDa. This failure is attributed to the low SNR, which renders orientation assignment unreliable. Furthermore, the reconstruction problem is high-dimensional and typical experiments involve hundreds of thousands of

DEPARTMENTS OF STATISTICS AND CCAM, UNIVERSITY OF CHICAGO, CHICAGO, IL, 60637, USA
 DEPARTMENTS OF STATISTICS AND CCAM, UNIVERSITY OF CHICAGO, CHICAGO, IL, 60637, USA
 PROGRAM IN APPLIED AND COMPUTATIONAL MATHEMATICS, PRINCETON UNIVERSITY, PRINCETON, NJ, 08544, USA
 PROGRAM IN APPLIED AND COMPUTATIONAL MATHEMATICS AND DEPARTMENT OF MATHEMATICS, PRINCETON UNIVERSITY, PRINCETON, NJ, 08544, USA
 DEPARTMENTS OF STATISTICS, UNIVERSITY OF CHICAGO, CHICAGO, IL, 60637, USA
E-mail addresses: jeremyhoskins@uchicago.edu, ykhoo@uchicago.edu, hm6655@princeton.edu, amits@math.princeton.edu, yuguanw@uchicago.edu.

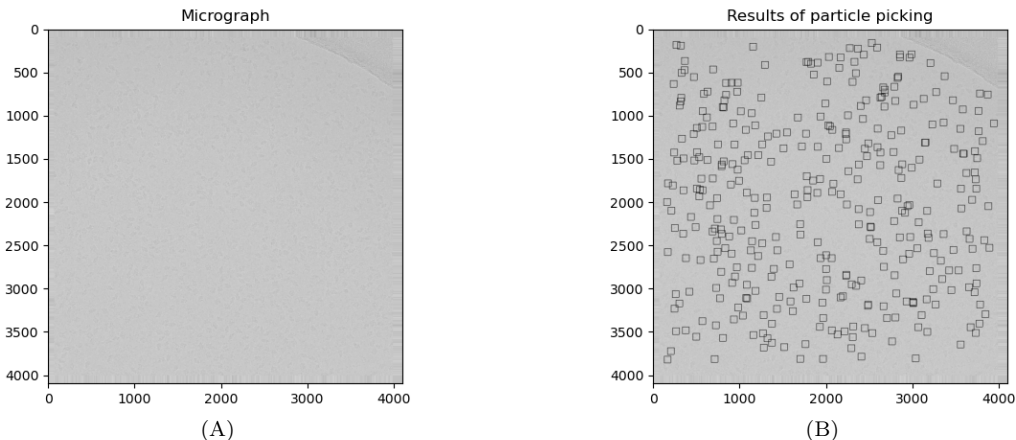


FIGURE 1. (A) A Cryo-EM micrograph from the Beta-galactosidase Falcon-II dataset [58]. (B) The result of the particle picking procedure using the APPLE picker [35] implemented in the ASPIRE software [74].

images, each of which must be used in every iteration of the refinement. This can be time-consuming and computationally expensive. In fact, the number of projection images required is inversely proportional to the signal-to-noise-ratio (SNR). Additionally, the optimization landscape of the likelihood is highly non-convex. To address these challenges, techniques such as stochastic optimization [51] have been proposed. Additionally, *ab initio* modeling [52, 63] is often required to obtain an initial structure close enough to the correct structure for iterative refinement.

The method of moments (MoM) approach for single particle reconstruction, proposed over forty years ago by Zvi Kam [38], is a promising approach for *ab initio* modeling. One particularly attractive feature of it is that it requires only low-order moments of the 2-D projection images of the volume. Given a large number of images, together with appropriate debiasing tools, the moments can be estimated quite accurately, making MoM less sensitive to noise compared to other *ab initio* approaches. Initially, Kam assumed a uniform distribution of the molecule orientations within the samples. However, he found that the second moment alone is insufficient and suggested certain slices of the third and fourth moments to improve performance. In general, the third-order moment is required in the case of uniform distribution of orientations [5]. However, *ab initio* modeling with only the second moment is still possible under uniformity when there are one or two noiseless projections provided [45, 37], which can be found by denoising the noisy images [61, 25, 11, 46]. More recent works [9, 8] also showed this possibility when the molecule is sparse, and certain sparsification is made during the reconstruction. Unfortunately, the uniform assumption is frequently invalid in practice, and the empirical orientations of the molecules can be quite non-uniform. Unlike the widespread belief that uniform distribution of orientation is optimal for reconstruction [4], non-uniformity is actually helpful, and it has been shown that the first two moments become sufficient for recovering a suitable approximation of the molecular structure if the distribution is known and very non-uniform [59]. It was also found in [59] that the distribution can be estimated jointly with the 3-D structure from the first two moments, but the resolution of the estimated structure is limited. For the iterative refinement approach, one can also sidestep the orientation estimation by matching the data in a distributional sense [33]. For a simpler but closely related problem called multi-reference alignment (MRA) [50, 54, 27] (that often serves as a mathematical abstraction of Cryo-EM without the projections), the third moment is required in the case of the uniform distribution, but the first two moments suffice for generic non-uniform distributions [2]. Additionally, higher order moments were found to be important for MRA when using the generalized method of moments [1] and 3-D reconstruction from images generated by X-ray free electron lasers (XFELs) [76]. Thus, one can hope that incorporating the third moment would significantly improve the quality of reconstruction in Cryo-EM for the case of an unknown non-uniform distribution of viewing orientations, which is our interest. In general, the third-order moment is not practically useful because it is too expensive to compute and too

large to store. The focus of this paper is to develop an efficient approach to compress and represent the third-order moment, without sacrificing the reconstruction quality.

We propose a flexible computational framework, called the subspace method of moments (subspace MoM), which enables joint reconstruction of the 3-D molecular structure (often referred to as “volume” by practitioners) and the unknown non-uniform distribution from a compressed representation of the first three moments, which are the *subspace moments*. Following [59], we assume the volume and the non-uniform distribution can be expanded using some basis functions. We project the sample moments computed from the noisy images into low-dimensional subspace moments, which are expressed as sums of simple rank-one components that can be evaluated efficiently. The coefficients of the volume and the non-uniform density are then reconstructed from the subspace moments through numerical optimization. We provide a particular choice of the basis functions, which serves as a baseline for subspace MoM. We also provide a way of finding subspaces by computing low-rank (tensor) decompositions of the second and the third moments using a randomized method. We illustrate our techniques on simulated datasets. The numerical experiments show that we can successfully obtain *ab-initio* models from the first three subspace moments when the distribution is non-uniform. Extending the numerical benchmarks to experimentally obtained projection images would require taking into account several factors that could potentially lead to inaccurately estimated moments. This includes the fact that the projection images can be imperfectly centered, that the particle picking procedure potentially can select non-particles, and the effect of aberrations through the so called contrast transfer function [48, 53, 71]. We defer these experimental considerations to future work. The MATLAB implementation of our method is publicly available at https://github.com/wangyuguan/subspace_MoM.

2. MATHEMATICAL PRELIMINARIES

In this section, we review some preliminaries necessary for describing our method. In Section 2.1, we first introduce convenient notations for representing and manipulating tensors. Following this, in Section 2.2, we discuss useful results from randomized linear algebra for matrix and tensor decompositions. Then in Section 2.3, we introduce the Cryo-EM model and the reconstruction problem considered in this paper. Finally, in Section 2.4, we conclude with a brief introduction to the method of moments in Cryo-EM.

2.1. Tensor notations. Let $M \in \mathbb{C}^{d_1 \times d_2 \times \dots \times d_n}$ be a tensor of order $n \geq 3$ where d_1, \dots, d_n are positive integers denoting the dimensions of the tensor. Let $U \in \mathbb{C}^{d_k \times r}$ be a matrix where $1 \leq k \leq n$. The *mode- k contraction* between the tensor M and the matrix U is defined as

$$(1) \quad (M \times_k U)_{i_1, \dots, i_{k-1}, j, i_{k+1}, \dots, i_n} = \sum_{i_k=1}^{d_k} M_{i_1, \dots, i_{k-1}, i_k, i_{k+1}, \dots, i_n} U_{i_k, j}$$

for $1 \leq i_1 \leq d_1, \dots, 1 \leq i_n \leq d_n$ and $1 \leq j \leq r$. The result of the contraction

$$M \times_k U \in \mathbb{C}^{d_1 \times \dots \times d_{k-1} \times r \times d_{k+1} \times \dots \times d_n}$$

is also a tensor of order n .

The *mode- k unfolding* of M is defined to be a matrix $M_{[k]} \in \mathbb{C}^{d_k \times \prod_{i \neq k}^n d_i}$ obtained by “flattening” all but the k -th dimension, and is denoted by

$$M_{[k]} = [M(i_k, i_{1:n} \setminus i_k)]_{i_k, i_{1:n} \setminus i_k}.$$

One standard tensor format is the *Tucker decomposition*. The Tucker decomposition [70] of the tensor M expresses M in terms of matrices $U^{(k)} \in \mathbb{C}^{d_k \times r_k}$ where $r_k \leq d_k, k = 1, \dots, n$ and a core tensor $M_c \in \mathbb{C}^{r_1 \times r_2 \times \dots \times r_n}$ by

$$(2) \quad M = M_c \times_1 U^{(1)} \times_2 U^{(2)} \times_3 \dots \times_n U^{(n)}.$$

In this paper, we further require the matrices $U^{(k)}, k = 1, \dots, n$ to have orthonormal columns. For each k , the matrix $U^{(k)}$ can be obtained by determining the range of the unfolding matrices $M_{[k]}$. Specifically, the columns of $U^{(k)}$ can be chosen to be an orthonormal basis of $\text{Range}(M_{[k]})$. Then clearly the following holds

$$(3) \quad U^{(k)} U^{(k)*} M_{[k]} = M_{[k]}.$$

This further implies that the core tensor M_c can be obtained by the formula

$$(4) \quad M_c = M \times_1 (U^{(1)})^* \times_2 (U^{(2)})^* \times_3 \dots \times_n (U^{(n)})^*.$$

In practice, rather than keeping the entire range of $M_{[k]}$, one seeks a good approximation with a much lower dimension. Typically, this is done via a truncated singular value decomposition (SVD), where $U^{(k)}$ represents the top left singular vectors. This procedure is called the higher-order singular value decomposition (HOSVD) [20]. Other methods for computing the Tucker decomposition include higher-order orthogonal iteration (HOOI) [21] and gradient-based optimization [24]. For details on tensor decomposition algorithms, see [43]. When the tensor $M \in \mathbb{C}^{d \times d \times \dots \times d}$ is symmetric, all the unfolding matrices coincide. In that case, we only need to carry out HOSVD on one unfolding matrix and obtain $U \in \mathbb{C}^{d \times r}$. Then we set $U^{(1)} = U^{(2)} = \dots = U^{(n)} = U$ in (4) with the resulting core tensor $M_c \in \mathbb{C}^{r \times r \times \dots \times r}$ also being symmetric.

Lastly, we define the Frobenius norm of a tensor $M \in \mathbb{C}^{d_1 \times d_2 \times \dots \times d_n}$ to be

$$(5) \quad \|M\|_F = \sqrt{\sum_{i_1, \dots, i_n=1}^{d_1, \dots, d_n} |M_{i_1, \dots, i_n}|^2}.$$

2.2. Randomized range finding algorithms. For large tensors, computing the truncated SVD of unfolding matrices can be prohibitively expensive. The randomized range-finding algorithm [34] efficiently finds an appropriate approximation $U^{(k)}$ via randomized sketching.

Consider a scenario where we have a large matrix $M \in \mathbb{C}^{d \times m}$, and our goal is to find a matrix $U \in \mathbb{C}^{d \times r}$ with $r \ll m, d$ such that

$$UU^*M \approx M.$$

In [34], the randomized range-finding algorithm is carried out in three steps:

- (1) Draw a random sketch matrix $S \in \mathbb{C}^{m \times r}$, for instance a Gaussian random matrix.
- (2) Form the $d \times r$ matrix $Y = MS$.
- (3) Compute U via the QR decomposition $Y = UR$.

The computational complexity of the randomized range-finding algorithm is only $O(mr + dmr + dr^2)$ compared to finding the range via a truncated SVD, which has complexity $O(md^2)$.

2.3. Introduction to the Cryo-EM Reconstruction Problem. We give a brief introduction to the Cryo-EM reconstruction problem. For a comprehensive introduction to this topic, we refer to [64, 6].

Let $V_\star : \mathbb{R}^3 \rightarrow \mathbb{R}$ denote the electrostatic potential created by a molecule, which we will refer to as the *volume* throughout the paper. We consider a simplified model of Cryo-EM by assuming perfect centering of the volume in the projected images and disregarding the effect of the aberrations of the projection images caused by the so-called contrast transfer function. We discuss approaches to take these effects into account in Section 5.

Under these two assumptions, the observed images, denoted by $I_j, j = 1, \dots, N$, are generated through

$$(6) \quad I_j(x, y) = \mathcal{I}[V_\star, R_j](x, y) + \epsilon_j(x, y), \quad (x, y) \in \mathcal{X}, \quad j = 1, \dots, N,$$

where \mathcal{X} denotes an $m \times m$ equispaced Cartesian 2-D grid, and

$$(7) \quad \mathcal{I}[V_\star, R_j](x, y) = \int_{\mathbb{R}} (R_j^{-1} \circ V_\star)(x, y, z) dz$$

denotes the noiseless 2-D projection generated by the volume V_\star and the 3-D rotation $R_j \in \mathcal{SO}(3)$. Here, R_j denotes the rotation matrix that is used to model the unknown viewing angle of the molecule in the j -th image and

$$(R_j^{-1} \circ V_\star)(x, y, z) := V_\star(R_j(x, y, z)^T)$$

denotes the rotation of V_\star by R_j^{-1} . Here, we use R_j^{-1} instead of R_j to rotate the volume so that in Section 3.3.1 we can directly use the results in [59] for modeling cryo-EM data. We assume that $\epsilon_j(\cdot)$ is an isotropic uncorrelated Gaussian random field (white noise) with variance σ^2 . In this paper, we assume σ^2 is known, and in practice, it can be estimated from the pixels in the corners of the projection images. The goal of Cryo-EM reconstruction is to reconstruct the unknown volume V_\star from the images $I_j, j = 1, \dots, N$. In a typical application, the sample size of images N is large, but the signal-to-noise ratio (SNR) is low.

We denote the Fourier transform of a function $f : \mathbb{R}^d \rightarrow \mathbb{R}$ by

$$(8) \quad \hat{f}(\xi) = \int_{\mathbb{R}^d} f(x) e^{-2\pi i \xi \cdot x} dx$$

where $\xi \in \mathbb{R}^d$ denotes the Fourier-space variable. For any 3-D volume $V : \mathbb{R}^3 \rightarrow \mathbb{R}$, the 2-D projection along the z axis is given by

$$I(x, y) = \int_{\mathbb{R}} V(x, y, z) dz$$

and the Fourier transform of $I(x, y)$ can be obtained from the Fourier transform of V by slicing through the origin of V parallel to the z axis, i.e.,

$$(9) \quad \hat{I}(\xi_x, \xi_y) = \hat{V}(\xi_x, \xi_y, \xi_z)|_{\xi_z=0}.$$

This is also known as the *Fourier slice theorem* [13] and implies that

$$(10) \quad \hat{\mathcal{I}}[V_\star, R_j](\xi_x, \xi_y) = (R_j^{-1} \circ \hat{V}_\star)(\xi_x, \xi_y, \xi_z)|_{\xi_z=0}$$

The image generation model can therefore be written in frequency space as

$$(11) \quad \hat{I}_j(\xi_x, \xi_y) = (R_j^{-1} \circ \hat{V}_\star)(\xi_x, \xi_y, \xi_z)|_{\xi_z=0} + \hat{\epsilon}_j(\xi_x, \xi_y).$$

Modeling the image formation model in frequency space is therefore easier than in real space, so it is conventional to reconstruct \hat{V} from \hat{I}_j and then transform the resulting volume to real space. In the rest of the paper, we will also refer to \hat{V} and $\hat{I}_1, \dots, \hat{I}_j$ as the volume and 2-D image data.

2.4. Method of moments in Cryo-EM. In this section, we introduce the main idea of the method of moments, which forms the basis of several recent reconstruction algorithms in Cryo-EM [59, 9, 37, 42, 7]. We assume that the 3-D rotation R , modeling the unknown viewing orientation, is drawn from some density μ over $\mathcal{SO}(3)$, which we will refer to as the *rotational density*. The first three moments of the Fourier 2-D projections (9) are functions given by

$$(12) \quad \mathcal{M}^{(1)}[V, \mu](\vec{\xi}) = \int_{\mathcal{SO}(3)} \hat{\mathcal{I}}[V, R](\vec{\xi}) \mu(R) dR,$$

$$(13) \quad \mathcal{M}^{(2)}[V, \mu](\vec{\xi}_1, \vec{\xi}_2) = \int_{\mathcal{SO}(3)} \hat{\mathcal{I}}[V, R](\vec{\xi}_1) \hat{\mathcal{I}}[V, R]^*(\vec{\xi}_2) \mu(R) dR,$$

$$(14) \quad \mathcal{M}^{(3)}[V, \mu](\vec{\xi}_1, \vec{\xi}_2, \vec{\xi}_3) = \int_{\mathcal{SO}(3)} \hat{\mathcal{I}}[V, R](\vec{\xi}_1) \hat{\mathcal{I}}[V, R](\vec{\xi}_2) \hat{\mathcal{I}}[V, R](\vec{\xi}_3) \mu(R) dR,$$

where $\vec{\xi}, \vec{\xi}_1, \vec{\xi}_2, \vec{\xi}_3 \in \mathbb{R}^2$ and dR denotes the *Haar measure* over $\mathcal{SO}(3)$ [18]. Note the complex conjugate in equation (13), which ensures that $\mathcal{M}^{(2)}$ is Hermitian in its matrix form. We assume that the volume V is band-limited, i.e., the Fourier transform of V is compactly supported in $[-1/2, 1/2]^3$. In this case, the $\vec{\xi}$'s in (12), (13) and (14) can be restricted to $[-1/2, 1/2]^2$. Using the Euler angle description of rotation matrices, we express the Haar measure as

$$(15) \quad dR = \frac{1}{8\pi^2} \sin \beta d\alpha d\beta d\gamma, \quad \alpha \in [0, 2\pi], \quad \beta \in [0, \pi], \quad \gamma \in [0, 2\pi],$$

where (α, β, γ) are the Euler angles with the ‘‘ZYZ convention’’. A brief introduction to Euler angles can be found in Appendix B.

Typically, we only observe the 2-D Fourier images on a set of $m \times m$ 2-D grid points $\xi \in \Xi$. Consequently, we treat the 2-D projection (9) evaluated on Ξ as a vector in \mathbb{C}^d where $d = m^2$ represents the number of pixels (image dimension). Similarly, the discretized first three moments have sizes $m^2, m^2 \times m^2$, and $m^2 \times m^2 \times m^2$, respectively. Throughout the paper, we use the vector $\hat{\mathcal{I}}[V, R](\Xi)$ to denote the evaluation of (9) on Ξ and the tensors $\mathcal{M}^{(k)}[V, R](\Xi^{\otimes k})$, for $k = 1, 2, 3$ to denote the evaluation of (12),(13),(14) on $\Xi^{\otimes k}$.

Let \hat{V}_\star and μ_\star denote the unknown ground truth volume and rotational density. For $k = 1, 2, 3$, we denote by $\overline{M}^{(k)} \in \mathbb{C}^d$ the sample estimates of the moments $\mathcal{M}^{(k)}[V_\star, \mu_\star](\Xi^{\otimes k})$. We provide the details of getting the estimates in Appendix A. Given these estimates, the method of moments (MoM) attempts to recover the ground truth (V_\star, μ_\star) by solving the optimization problem:

$$(16) \quad \min_{V, \mu} \sum_{k=1}^3 \lambda_k \|\mathcal{M}^{(k)}[V, \mu](\Xi^{\otimes k}) - \overline{M}^{(k)}\|_F^2.$$

Here, $\lambda_k \geq 0$ are suitably chosen weights. In practice, finding the global minima of (16) is challenging due to its non-convexity and the significant computational cost of forming the moments. For instance, forming the

empirical third-order moment from the data costs $O(Nd^3)$ where d denotes the number of pixels in an image and N the number of images used in estimating the moments. Addressing these computational challenges in MoM is the central focus of this paper.

3. SUBSPACE METHOD OF MOMENTS

In this section, we introduce our main contribution: an efficient algorithm for solving the method of moments. Firstly, we consider the case in which approximations of the ranges of the unfolding matrices of the estimated moments are provided. For $k = 1, 2, 3$, we denote by $U^{(k)} \in \mathbb{C}^{d \times r_k}$, $r_k \ll d$ the basis matrices of the ranges, with orthogonal columns. Intuitively, our approach relies on compressing the estimated moments using the Tucker decomposition, as in equation (2). More precisely, one can apply projection operators $\mathcal{P}_{U^{(k)}}^{(k)} : (\mathbb{C}^d)^{\otimes k} \rightarrow (\mathbb{C}^{r_k})^{\otimes k}$, for $k = 1, 2, 3$, to the estimated moments as follows:

$$(17) \quad \mathcal{P}_{U^{(1)}}^{(1)}(\overline{M}^{(1)}) = (U^{(1)})^* \overline{M}^{(1)},$$

$$(18) \quad \mathcal{P}_{U^{(2)}}^{(2)}(\overline{M}^{(2)}) = (U^{(2)})^* \overline{M}^{(2)} (U^{(2)}),$$

$$(19) \quad \mathcal{P}_{U^{(3)}}^{(3)}(\overline{M}^{(3)}) = \overline{M}^{(3)} \times_1 U^{(3)} \times_2 U^{(3)} \times_3 U^{(3)}.$$

By doing so, we obtain compressed representations of the estimated moments, which significantly reduces their sizes, especially the size of $\overline{M}^{(3)}$ which is reduced from $O(d^3)$ to $O(r_3^3)$. Similarly, we compress the moments $\mathcal{M}^{(k)}[V, \mu](\Xi^{\otimes k})$, for $k = 1, 2, 3$ formed by the volume \hat{V} and rotational density μ , using the operators $\mathcal{P}_{U^{(k)}}^{(k)}$. We refer to the resulting compressed moments $\mathcal{M}_c^{(k)}[V, \mu](\Xi^{\otimes k}) = \mathcal{P}_{U^{(k)}}^{(k)}(\mathcal{M}^{(k)}[V, \mu](\Xi^{\otimes k}))$, for $k = 1, 2, 3$ as the *subspace moments*.

Using these compressed representations, we can replace our original MoM problem (16) by a reduced problem, given by

$$(20) \quad \min_{V, \mu} \sum_{k=1}^3 \lambda_k \|\mathcal{P}_{U^{(k)}}^{(k)}(\mathcal{M}^{(k)}[V, \mu](\Xi^{\otimes k})) - \mathcal{P}_{U^{(k)}}^{(k)}(\overline{M}^{(k)})\|_F^2.$$

We refer to solving this problem as the *subspace method of moments (subspace MoM)*. A similar approach has also been used in iterative refinement algorithms, where it is referred to as *subspace EM* [23]. If $r_k = d$, the matrices $U^{(k)}$ are basis matrices of the entire ranges of the moments, so the operators $\mathcal{P}_{U^{(k)}}^{(k)}$ are invertible and the optimization problem in (20) is equivalent to (16). On the other hand, if $r_k < d$, the operators $\mathcal{P}_{U^{(k)}}^{(k)}$ are not invertible, so the optimization problem in (20) is not equivalent to (16). However, using the orthogonality of the columns of the $U^{(k)}$, we have

$$(21) \quad \|\mathcal{P}_{U^{(k)}}^{(k)}(\mathcal{M}^{(k)}[V, \mu](\Xi^{\otimes k})) - \mathcal{P}_{U^{(k)}}^{(k)}(\overline{M}^{(k)})\|_F^2 \leq \|\mathcal{M}^{(k)}[V, \mu](\Xi^{\otimes k}) - \overline{M}^{(k)}\|_F^2.$$

Similarly, we have

$$(22) \quad \begin{aligned} \|\mathcal{M}^{(k)}[V, \mu](\Xi^{\otimes k}) - \overline{M}^{(k)}\|_F &\leq \|\mathcal{P}_{U^{(k)}}^{(k)}(\mathcal{M}^{(k)}[V, \mu](\Xi^{\otimes k})) - \mathcal{P}_{U^{(k)}}^{(k)}(\overline{M}^{(k)})\|_F \\ &+ \|\mathcal{P}_{U^{(k)}}^{(k)\perp}(\mathcal{M}^{(k)}[V, \mu](\Xi^{\otimes k}))\|_F + \|\mathcal{P}_{U^{(k)}}^{(k)\perp}(\overline{M}^{(k)})\|_F \end{aligned}$$

where the error terms $\mathcal{P}_{U^{(k)}}^{(k)\perp}$ denotes the projection operator orthogonal to $\mathcal{P}_{U^{(k)}}^{(k)}$ for $k = 1, 2, 3$. In particular, we have

$$(23) \quad \mathcal{P}_{U^{(1)}}^{(1)\perp}(\overline{M}^{(1)}) = (I_d - U^{(1)}(U^{(1)})^*)\overline{M}^{(1)},$$

$$(24) \quad \mathcal{P}_{U^{(2)}}^{(2)\perp}(\overline{M}^{(2)}) = (I_d - U^{(2)}(U^{(2)})^*)\overline{M}^{(2)}(I_d - U^{(2)}(U^{(2)})^*),$$

$$(25) \quad \mathcal{P}_{U^{(3)}}^{(3)\perp}(\overline{M}^{(3)}) = \overline{M}^{(3)} \times_1 (I_d - U^{(3)}(U^{(3)})^*) \times_2 (I_d - U^{(3)}(U^{(3)})^*) \times_3 (I_d - U^{(3)}(U^{(3)})^*).$$

If $U^{(1)} = I_d$ and the equation (2) approximately holds for $\overline{M}^{(k)}$ with the range matrices given by the provided $U^{(k)}$ and the core tensor given by $\mathcal{P}_{U^{(k)}}^{(k)}(\overline{M}^{(k)})$ when $k = 2, 3$, the term $\sum_{k=1}^3 \lambda_k \|\mathcal{P}_{U^{(k)}}^{(k)\perp}(\overline{M}^{(k)})\|_F^2$ is small. The gap between the two problems is then approximately given by the term

$$\lambda_2 \|\mathcal{P}_{U^{(2)}}^{(2)\perp}(\mathcal{M}^{(2)}[V, \mu](\Xi^{\otimes 2}))\|_F^2 + \lambda_3 \|\mathcal{P}_{U^{(3)}}^{(3)\perp}(\mathcal{M}^{(3)}[V, \mu](\Xi^{\otimes 3}))\|_F^2.$$

In order to solve (20), we further need to discretize the problem. We assume that the volume \hat{V} and the rotational density μ are expanded in some suitable bases. The integrals over $\mathcal{SO}(3)$ in (12),(13) and (14) can be approximated via numerical quadrature. In addition to yielding numerical approximations of the moments, using quadrature has another advantage: it provides a natural approximate decomposition of $\mathcal{M}^{(k)}[V, \mu], k = 1, 2, 3$, as a sum of rank 1 tensors, which is crucial to our approach. The details of forming the subspace MoM problem in terms of some basis and numerical integration are provided in Section 3.1. Then in Section 3.2, we provide a way of determining the projection operators $\mathcal{P}_{U^{(k)}}^{(k)}$ via a randomized range finding algorithm. In Section 3.3, we discuss additional details regarding the optimization of (20).

3.1. Details of the reduced moment problem. In the first part of this section (Section 3.1.1), we present an approach for efficiently discretizing the reduced moment problem and evaluating the cost function. In the second part (Section 3.1.2), we describe an efficient method for obtaining the subspace moments.

3.1.1. Compressed representation of moments. We assume that the Fourier transform of the volume and the rotational density can be represented by suitable basis functions, as in:

$$(26) \quad \hat{V}_a(\xi_x, \xi_y, \xi_z) = \sum_{i \in \mathcal{S}_V} a_i \phi_i(\xi_x, \xi_y, \xi_z),$$

$$(27) \quad \mu_b(R) = \sum_{j \in \mathcal{S}_\mu} b_j \psi_j(R).$$

Here, $\phi_i : \mathbb{R}^3 \rightarrow \mathbb{C}$ and $\psi_j : \mathcal{SO}(3) \rightarrow \mathbb{C}$ are basis functions with index sets \mathcal{S}_V and \mathcal{S}_μ . The coefficients $a \in \mathbb{C}^{|\mathcal{S}_V|}$ and $b \in \mathbb{C}^{|\mathcal{S}_\mu|}$ are the expansion coefficients, subject to additional constraints to ensure that \hat{V}_a is the Fourier transform of a real-valued 3-D volume and μ_b is a probability density over $\mathcal{SO}(3)$. Specific examples of suitable basis functions and constraints for the coefficients are provided in Section 3.3.1 and Section 3.3.2.

Using the Fourier slice theorem (9), the noiseless 2-D projection generated by the volume \hat{V}_a and 3-D rotation R is given by

$$(28) \quad \hat{\mathcal{I}}[V_a, R](\xi_x, \xi_y) = \sum_{i \in \mathcal{S}_V} a_i (R^{-1} \circ \phi_i)(\xi_x, \xi_y, 0)$$

where $(\xi_x, \xi_y) \in \Xi$. For any $R \in \mathcal{SO}(3)$, we define the $d \times |\mathcal{S}_V|$ matrix $\Phi[R, \Xi]$ by

$$(\Phi[R, \Xi])_{i,j} = (R^{-1} \circ \phi_j)(\vec{\xi}_i, 0),$$

for $\vec{\xi}_i \in \Xi, i = 1, \dots, d$ and $j \in \mathcal{S}_V$. Using this notation, we can represent the 2-D projection in (28) by matrix-vector multiplication:

$$(29) \quad \hat{\mathcal{I}}[V_a, R](\Xi) = \Phi[R, \Xi]a.$$

To represent the rotational density in a succinct form, we define the mapping $\Psi : \mathcal{SO}(3) \rightarrow \mathbb{C}^{1 \times |\mathcal{S}_\mu|}$ by

$$(\Psi[R])_j = \psi_j(R),$$

for $j \in \mathcal{S}_\mu$, allowing us to rewrite (27) as

$$(30) \quad \mu_b(R) = \Psi[R]b.$$

Inserting the equations (29) and (30) into the definitions of the moments given in (12), (13) and (14), we obtain the moments $\mathcal{M}^{(k)}[a, b](\Xi^{\otimes k})$ expressed in terms of expansion coefficients a and b . In detail, we obtain

$$(31) \quad \mathcal{M}^{(1)}[a, b](\Xi) = \int_{\mathcal{SO}(3)} (\Phi[R, \Xi]a)(\Psi[R]b) \, dR,$$

$$(32) \quad \mathcal{M}^{(2)}[a, b](\Xi^{\otimes 2}) = \int_{\mathcal{SO}(3)} (\Phi[R, \Xi]a)(\Phi[R, \Xi]a)^*(\Psi[R]b) \, dR,$$

$$(33) \quad \mathcal{M}^{(3)}[a, b](\Xi^{\otimes 3}) = \int_{\mathcal{SO}(3)} (\Phi[R, \Xi]a)^{\otimes 3}(\Psi[R]b) \, dR.$$

The subspace moments are then given by

$$\mathcal{M}_c^{(k)}[a, b](\Xi^{\otimes k}) = \mathcal{P}_{U^{(k)}}^{(k)}(\mathcal{M}^{(k)}[a, b](\Xi^{\otimes k})), \quad k = 1, 2, 3$$

where the projection operators $\mathcal{P}_{U^{(k)}}^{(k)}$, for $k = 1, 2, 3$ are given in (17), (18) and (19).

We use a numerical quadrature to evaluate the integrals over $\mathcal{SO}(3)$, with quadrature weights and nodes denoted by $\{(w_i, R_i), i = 1, \dots, Q\}$ for $w_i > 0$ and $R_i \in \mathcal{SO}(3)$. We can approximate the moments by

$$\begin{aligned} \mathcal{M}^{(1)}[a, b](\Xi) &\approx \sum_{i=1}^Q w_i (\Phi[R_i, \Xi]a)(\Psi[R_i]b), \\ \mathcal{M}^{(2)}[a, b](\Xi^{\otimes 2}) &\approx \sum_{i=1}^Q w_i (\Phi[R_i, \Xi]a)(\Phi[R_i, \Xi]a)^*(\Psi[R_i]b), \\ \mathcal{M}^{(3)}[a, b](\Xi^{\otimes 3}) &\approx \sum_{i=1}^Q w_i (\Phi[R_i, \Xi]a)^{\otimes 3}(\Psi[R_i]b). \end{aligned}$$

It is possible to construct highly accurate quadrature formulas when the basis functions are chosen appropriately. However, these can be expensive to evaluate and it is more practical to use inexact quadrature. In particular, it has also been demonstrated in [42] that good *ab initio* models can be obtained from the first two moments when inexact quadrature is used in the reconstruction step. More evidences are provided in Section 4.2 of this paper.

Using the same quadrature rule, we can approximate the subspace moments by

$$(34) \quad \mathcal{M}_c^{(1)}[a, b](\Xi) \approx \sum_{i=1}^Q w_i ((U^{(1)})^* \Phi[R_i, \Xi]a)(\Psi[R_i]b),$$

$$(35) \quad \mathcal{M}_c^{(2)}[a, b](\Xi^{\otimes 2}) \approx \sum_{i=1}^Q w_i ((U^{(2)})^* \Phi[R_i, \Xi]a)((U^{(2)})^* \Phi[R_i, \Xi]a)^*(\Psi[R_i]b),$$

$$(36) \quad \mathcal{M}_c^{(3)}[a, b](\Xi^{\otimes 3}) \approx \sum_{i=1}^Q w_i ((U^{(3)})^* \Phi[R_i, \Xi]a)^{\otimes 3}(\Psi[R_i]b).$$

The estimated subspace moments $\overline{M}_c^{(k)} = \mathcal{P}_{U^{(k)}}^{(k)}(\overline{M}^{(k)})$, for $k = 1, 2, 3$, can be obtained from the data using the method in Section 3.1.2. The subspace MoM problem, initially defined in (20), can be rewritten as an optimization problem over the expansion coefficients (a, b) , given by

$$(37) \quad \min_{a, b} \sum_{k=1}^3 \lambda_k \|\mathcal{M}_c^{(k)}[a, b](\Xi^{\otimes k}) - \overline{M}_c^{(k)}\|_F^2$$

where the subspace moments $\mathcal{M}_c^{(k)}[a, b](\Xi^{\otimes k})$ are evaluated using equations (34), (35) and (36). In this paper, we choose the weights to be $\lambda_k = \frac{1}{\|\overline{M}_c^{(k)}\|_F^2}$, which is equivalent to minimizing the relative distances to the estimated moments with the same weights. See [59, 7] for other possible choices of weights. The algorithm in this paper can be easily modified to accommodate these choices, but we find that the current choice gives much quicker convergence compared to the others.

We now analyze the time complexity of evaluating the cost function in (37). The constant terms $(U^{(k)})^* \Phi[R_i, \Xi] \in \mathbb{C}^{r_k \times |\mathcal{S}_V|}$, for $k = 1, 2, 3$, and $i = 1, \dots, Q$ as well as $\Psi[R_i] \in \mathbb{C}^{1 \times |\mathcal{S}_\mu|}$, for $i = 1, \dots, Q$ can be precomputed and stored for repeated use. The time complexity needed to store the results of precomputation is $O(Q|\mathcal{S}_\mu|(d+1)\sum_{k=1}^3 r_k)$ and the space complexity is $O(Q|\mathcal{S}_V|\sum_{k=1}^3 r_k + Q|\mathcal{S}_\mu|)$. In Section 3.3.1, we provide details for the specific choice of basis used in our implementation and in particular bound $|\mathcal{S}_\mu|$ and $|\mathcal{S}_V|$ in terms of the truncation limits for those bases.

In each evaluation, we compute the matrix-vector multiplications $\{(U^{(k)})^* \Phi[R_i, \Xi]a\} \in \mathbb{C}^{r_k}$ and $\Psi[R_i]b \in \mathbb{C}$, which has time complexity $O(Q|\mathcal{S}_V|(r_1 + r_2 + r_3) + Q|\mathcal{S}_\mu|)$. Then for each $k = 1, 2, 3$, we form the k -th order vector outer product of each computed $\{(U^{(k)})^* \Phi[R_i, \Xi]a\}$, and multiply the result with the weight $w_i(\Psi[R_i]b)$, and form the subspace moments on the fly, resulting in a total time complexity of

$O(Q(r_1 + r_2^2 + r_3^3))$. Lastly, we compute the Frobenius distances between the subspace moments and the estimated moments, which has a time complexity $O(r_1 + r_2^2 + r_3^3)$. The overall computational complexity is $O\left(Q\left(|\mathcal{S}_V||\mathcal{S}_\mu|\sum_{k=1}^3 r_k + \sum_{k=1}^3 r_k^k + |\mathcal{S}_\mu|\right)\right)$. The evaluation of the gradient of the cost function in (37) has the same time complexity, and we omit the details here.

Remark. For clarity, we have assumed all the subspace moments are evaluated using the same quadrature rule as described in Section 3.1.1. In practice, the number of quadrature nodes used to integrate the third subspace moments may be larger than those used in the quadrature rules for the first two subspace moments. See Appendix B for a discussion on constructing different quadrature rules for the first three moments when the basis functions are chosen according to Section 3.3.1.

3.1.2. *Estimating subspace moments from data.* In this section, we discuss a reduced-complexity method to forming the subspace moments $\overline{M}_c^{(k)}$, for $k = 1, 2, 3$. We assume the subspaces determined by the matrices $U^{(k)} \in \mathbb{C}^{d \times r_k}$ are given, and the process of finding them will be discussed in the next section (Section 3.2).

For clarity, we assume that the data $\hat{I}_j = \hat{\mathcal{I}}[V_\star, R_j](\Xi)$, for $j = 1, \dots, N$ is noiseless, and recall that \hat{V}_\star represents the ground truth volume. In the case of noisy data, we debias the estimated subspace moments during their formation (refer to Appendix A for details). In practice, we may need to pre-process the images before moment estimation, by for instance applying filters to the images. The details of this procedure are provided in Appendix A. For clarity of notation, we assume in the following that pre-processing has already been applied to the \hat{I}_j . To illustrate, we consider the formation of the estimated subspace third moment given by

$$(38) \quad \overline{M}^{(3)} = \frac{1}{N} \sum_{j=1}^N \hat{I}_j^{\otimes 3}.$$

Applying the projection operator in (19), we obtain

$$(39) \quad \overline{M}_c^{(3)} = \frac{1}{N} \sum_{j=1}^N \mathcal{P}_{U^{(3)}}^{(3)}(\hat{I}_j^{\otimes 3})$$

$$(40) \quad = \frac{1}{N} \sum_{j=1}^N ((U^{(3)})^* \hat{I}_j)^{\otimes 3}.$$

Examining the right-hand side of (40), we observe that for each I_j where $j = 1, \dots, N$, we can initially compute $(U^{(3)})^* \hat{I}_j$ and form $((U^{(3)})^* \hat{I}_j)^{\otimes 3}$, and then add the summands up. By doing so, the total time complexity is only $O(Ndr_3 + Nr_3^3)$. This computational strategy, commonly referred to as “streaming” [67, 69], avoids the explicit formation of $\overline{M}^{(3)} \in \mathbb{C}^{d \times d \times d}$, which would necessitate $O(Nd^3)$ operations.

The formation of the estimated first two moments is computationally and conceptually simpler, and is given by

$$(41) \quad \overline{M}_c^{(1)} = \frac{1}{N} \sum_{j=1}^N (U^{(1)})^* \hat{I}_j,$$

$$(42) \quad \overline{M}_c^{(2)} = \frac{1}{N} \sum_{j=1}^N ((U^{(2)})^* \hat{I}_j)((U^{(2)})^* \hat{I}_j)^*.$$

They can be formed simultaneously with the calculation of $\overline{M}_c^{(3)}$, resulting in a total time complexity of only $O(Nd(r_1 + r_2) + N(r_1 + r_2^2))$.

3.2. **Finding subspaces by random sketching.** To determine the matrices $U^{(k)} \in \mathbb{C}^{d \times r_k}$, for $k = 1, 2, 3$, used in the previous sections (Section 3.1.1, Section 3.1.2), we use a specific type of randomized range finding algorithm (in Section 2.2). This algorithm is applied to the unfolding matrices $\overline{M}^{(2)} \in \mathbb{C}^{d \times d}$ and $\overline{M}_{[1]}^{(3)} \in \mathbb{C}^{d \times d^2}$. For clarity, we assume noiseless data, as discussed in Section 3.1.2.

To sketch the empirical second moment, given by

$$(43) \quad \overline{M}^{(2)} = \frac{1}{N} \sum_{j=1}^N \hat{I}_j \hat{I}_j^*,$$

we apply a Gaussian random matrix $G \in \mathbb{C}^{d \times s}$ with $s < d$ being a sufficiently large sampling size. The resulting smaller matrix of size $d \times s$ is then computed as

$$(44) \quad \overline{M}^{(2)} G = \frac{1}{N} \sum_{j=1}^N \hat{I}_j (G^* \hat{I}_j)^*.$$

This computation achieved through streaming involves only $O(Nds)$ operations. When the sampling size s is sufficiently large, the range of $\overline{M}^{(2)} G$ approximates the range of $\overline{M}^{(2)}$. To select the bases in a data-dependent way, we obtain the SVD of $\overline{M}^{(2)} G$ and denote the singular values by $\sigma_1^{(2)} \geq \sigma_2^{(2)} \geq \dots \geq \sigma_s^{(2)} \geq 0$. We determine $r_2 > 0$, the dimension of the subspace for compressing the $\overline{M}^{(2)}$ to be the first r such that

$$(45) \quad \frac{\sum_{i=1}^r (\sigma_i^{(2)})^2}{\sum_{i=1}^s (\sigma_i^{(2)})^2} > 1 - \tau^{(2)}$$

where $\tau^{(2)} > 0$ is a small value. The range matrix $U^{(2)} \in \mathbb{C}^{d \times r_2}$ of the subspace is formed by the corresponding first r_2 left singular vectors.

For the third estimated moment, sketching its unfolding matrix $\overline{M}_{[1]}^{(3)} \in \mathbb{C}^{d \times d^2}$ with a Gaussian random matrix of size $d^2 \times s$ through streaming incurs a complexity of $O(Nd^2s)$, which is still expensive. To alleviate this, we use a structured tensor sketch operator [3, 68, 67], denoted by $\mathcal{S}[G^{(1)}, G^{(2)}] : \mathbb{C}^{d \times d^2} \rightarrow \mathbb{C}^{d \times s}$. Generated by two independent Gaussian random matrices $G^{(1)}, G^{(2)} \in \mathbb{R}^{d \times s}$, this operator allows us to sketch $\overline{M}_{[1]}^{(3)}$ with reduced complexity, given by

$$(46) \quad \mathcal{S}[G^{(1)}, G^{(2)}](\overline{M}_{[1]}^{(3)}) = \frac{1}{N} \sum_{j=1}^N \hat{I}_j \left[((G^{(1)})^T \hat{I}_j) \odot ((G^{(2)})^T \hat{I}_j) \right]$$

where \odot denotes the element-wise product of vectors. Notably, the sketch operation in (46) is equivalent to sketching $\overline{M}_{[1]}^{(3)}$ using a $d^2 \times s$ random sketch matrix with correlated entries. In practice, this sketch operator provides sufficient randomness for column sampling. Subsequently, we compute the SVD of $\mathcal{S}[G^{(1)}, G^{(2)}](\overline{M}_{[1]}^{(3)})$ to obtain the singular values $\sigma_1^{(3)} \geq \sigma_2^{(3)} \geq \dots \geq \sigma_s^{(3)} \geq 0$ and the corresponding left singular vectors. Similarly, we determine r_3 , the dimension of the subspace for compressing $\overline{M}^{(3)}$, to be the first r such that

$$(47) \quad \frac{\sum_{i=1}^r (\sigma_i^{(3)})^2}{\sum_{i=1}^s (\sigma_i^{(3)})^2} > 1 - \tau^{(3)}$$

for some small value $\tau^{(3)} > 0$. The range matrix $U^{(3)}$ of the subspace is formed by the corresponding first r_3 singular vectors.

The parameters s , $\tau^{(2)}$, and $\tau^{(3)}$ need to be specified before running the estimating procedure. Larger s and smaller $\tau^{(2)}, \tau^{(3)}$ give a better approximation to the moments but also incur greater computational cost. The effect of varying $\tau^{(2)}$ and $\tau^{(3)}$ is discussed in Section 4.1.

Remark. *The first moment, $\overline{M}^{(1)}$, does not contribute useful information for compression. Therefore, in practice, we compress the first moment using $U^{(2)}$, which implies that $r_1 = r_2$. During reconstruction, we apply the same quadrature formula to integrate both the first and second subspace moments, eliminating the need for additional precomputation of the first moment, which helps saving memory.*

3.2.1. Data augmentation in the presence of symmetry. There are other ways to obtain the subspaces. For example, we can choose the 2-D Fourier-Bessel basis to expand the images, a method commonly used to compress images in Cryo-EM [78]. However, the Fourier-Bessel expansion may be redundant and sparse. Therefore, a step of principal component analysis is typically employed, often referred to as *steerable PCA*. There are fast algorithms for expanding images and performing steerable PCA including [77, 47, 46].

We highlight that steerable PCA can also be accelerated using randomized sketching. Assuming that the clean images $\hat{\mathcal{I}}[V, R]$ are represented in polar coordinates (r, θ) , where $0 \leq r \leq A$, $\theta \in [0, 2\pi]$, and A denotes the radius of the images, we can represent the second moment as

$$\mathcal{M}^{(2)}[V, R]((r, \theta), (r', \theta')) = \int_{\mathcal{SO}(3)} \hat{\mathcal{I}}[V, R](r, \theta) \hat{\mathcal{I}}^*[V, R](r', \theta') \mu(R) dR.$$

In Cryo-EM, it is useful to assume the rotational distribution $\mu(R)$ is invariant to *in-plane rotations*- meaning that the distribution is invariant under (two-dimensional) rotations of all the 2-D projections. Physically, this in-plane invariance is a natural assumption, as there is no a priori reason to assume a preferred direction in the 2-D projection plane. Even if this does not hold in a particular dataset, we can achieve this by simply augmenting the given projection images by also including their in-plane rotations. Under this assumption, we have

$$\mathcal{M}^{(2)}[V, \mu]((r, \theta), (r', \theta')) = \mathcal{M}^{(2)}[V, \mu]((r, \theta + \varphi), (r', \theta' + \varphi))$$

for any $\varphi \in [0, 2\pi]$. Therefore, we have

$$\mathcal{M}^{(2)}[V, \mu]((r, \theta), (r', \theta')) = \frac{1}{2\pi} \int_0^{2\pi} \mathcal{M}^{(2)}[V, \mu]((r, \theta + \varphi), (r', \theta' + \varphi)) d\varphi,$$

which can be used to show that the second moment is a block-diagonal matrix when the images are represented by Fourier-Bessel functions [46]. Importantly, it inherently provides a method for data augmentation by adding in-plane rotations of the images to the dataset, yielding a more accurately estimated second moment.

The key step in sketching the second moment is numerically evaluating the integrals

$$(48) \quad \int_0^A \int_0^{2\pi} \mathcal{M}^{(2)}[V, \mu]((r, \theta), (r', \theta')) G_i(r', \theta') r' dr' d\theta', \quad j = 1, \dots, s.$$

Here, $G_i(r', \theta')$, for $i = 1, \dots, s$, represents s random sketch functions. Equation (48) is the continuous analogue of multiplying the second moment matrix by a random matrix with s columns. We can numerically evaluate a sketched quantity by

$$(49) \quad \begin{aligned} g_i[V, R](\varphi) &= \int_0^{2\pi} \int_0^A \hat{\mathcal{I}}^*[V, R](r', \theta' + \varphi) G_i(r', \theta') r' dr' d\theta' \\ &= \int_0^{2\pi} \int_0^A \hat{\mathcal{I}}^*[V, R](r', \theta') G_i(r', \theta' - \varphi) r' dr' d\theta'. \end{aligned}$$

The i -th column of the sketched second moment is then obtained as

$$(50) \quad (G \circ \mathcal{M}^{(2)})_i[V, R](r, \theta) = \frac{1}{2\pi} \int_{\mathcal{SO}(3)} \left(\int_0^{2\pi} \hat{\mathcal{I}}[V, R](r, \theta + \varphi) g_i[V, R](\varphi) d\varphi \right) \mu(R) dR.$$

Besides the invariance to in-plane rotations, it is also useful to assume that the rotational distribution μ is invariant to in-plane reflection, which implies $\mu(R) = \mu(RJ)$ for all $R \in \mathcal{SO}(3)$ where $J = \text{diag}(1, -1, -1)$. In that case, we can augment the dataset with reflected copies of all images so that the estimated moments always have the relevant symmetry.

Remark. We would like to describe an approach of sketching the symmetrized moments in (50) that could be more efficient compared to data augmentation. Empirically, we aim to compute

$$(51) \quad (G \circ \overline{\mathcal{M}^{(2)}})_i = \frac{1}{2\pi} \int_0^{2\pi} \sum_{j=1}^N R(\varphi) \hat{I}_j \hat{I}_j^* R(-\varphi) G_i d\varphi$$

where $R(\varphi) \in \mathbb{C}^{d \times d}$ is a linear operator that rotates I_j by $\varphi \in [0, 2\pi]$, satisfying $R(-\varphi) = R(\varphi)^*$, and $G_i \in \mathbb{C}^{d \times 1}$ is a sketch vector. By choosing $G_i = FW^{(i)}$, where $F \in \mathbb{C}^{d \times B}$ has columns composed of B Fourier-Bessel basis functions of degree at most L , and $W^{(i)} \in \mathbb{C}^{B \times 1}$ is a random sketch vector, we use the properties of the steerable basis to obtain $R(-\varphi)F = FD(\varphi)$, where $D(\varphi) \in \mathbb{C}^{B \times B}$ is a diagonal matrix with

entries $e^{-iL\varphi}, e^{-i(L-1)\varphi}, \dots, e^{iL\varphi}$. Using a projection method based on the trapezoidal rule with $L+1$ points, we can numerically compute a coefficient matrix $A^{(i)} \in \mathbb{C}^{d \times (2L+1)}$ such that

$$(52) \quad \frac{1}{N} \sum_{j=1}^N \hat{I}_j \left(\hat{I}_j^* (FD(\varphi)W) \right) = A^{(i)} E(\varphi)$$

where $E(\varphi) \in \mathbb{C}^{(2L+1) \times 1}$ consists of the Fourier basis elements $[e^{-iL\varphi}, e^{-i(L-1)\varphi}, \dots, e^{iL\varphi}]^T$. The computational complexity of this step is $O(NdL)$. Once $A^{(i)}$ is computed, the cost of numerically evaluating

$$(53) \quad (G \circ \overline{\mathcal{M}^{(2)}})_i = \frac{1}{2\pi} \int_0^{2\pi} R(\varphi) A^{(i)} E(\varphi) d\varphi$$

is reduced to $O(QdL)$ where Q is the number of quadrature nodes used for integrating φ . In the general case, where we have r sketch vectors, the total complexity of the method is $O(NdLr + QdLr)$, and it is parallelizable. While performing data augmentation has complexity $O(NdQr)$, which is more expensive when Q is large. Typically, we choose a moderate L for ab-initio modeling to extract smooth features, and a large $Q \approx \sqrt{d}$ to capture all possible in-plane rotations as well as achieve denoising effect. This approach can be naturally extended to sketch the third moment, and we omit those details here.

3.3. Choice of basis and additional optimization details. In this section, we discuss the optimization method used to solve the subspace MoM problem (37). In Section 3.3.1, we specify our choice of basis functions used for representing the volume and rotational density. It is important to note that we require \hat{V} to be the Fourier transform of a real-valued function and μ to be a probability density. Once the basis is chosen, these requirements correspond to constraints on the coefficients of the basis. We explain how to construct and enforce these constraints in the optimization problem in Section 3.3.2. Then, in Section 3.3.3, we propose a two-stage optimization approach [39], which in practice performs better than directly solving the full problem (37).

3.3.1. Choice of basis. Since we have assumed that the volume is bandlimited by $1/2$ in Section 2.4, we can represent the Fourier transform of the volume in a spherical Bessel basis $\phi_{l,m,s}$, where

$$(54) \quad \phi_{l,m,s}(\rho, \theta, \varphi) = c_{l,s} \cdot j_l \left(\rho \frac{z_{l,s}}{1/2} \right) Y_l^m(\theta, \varphi).$$

Here, the angular part of the basis (54) is modeled by the spherical harmonics

$$(55) \quad Y_l^m(\theta, \varphi) = \sqrt{\frac{2l+1}{4\pi} \frac{(l-m)!}{(l+m)!}} P_l^m(\cos \theta) e^{im\varphi}$$

with $l \geq 0$, $-l \leq m \leq l$, where P_l^m are the associated Legendre functions [14]. Recall that the spherical harmonics form an orthogonal basis with respect to the measure $\sin \theta d\theta d\varphi$ on the unit sphere. The radial part of the basis (54) consists of spherical Bessel functions, where j_l denotes the l -th degree spherical Bessel function [14], and $z_{l,s}$ is the s -th zero of j_l . This set of functions also forms an orthogonal basis on $[0, 1/2]$ with respect to the measure $\rho^2 d\rho$. The constants $c_{l,s}$ are chosen such that the functions $\phi_{l,m,s}$ are normalized and therefore form an orthonormal basis with respect to the measure $\rho^2 \sin \theta d\rho d\theta d\varphi$. In particular, the basis functions $\phi_{l,m,s}$ are the eigenfunctions of the Laplacian operator in a 3-D ball of radius $1/2$ with Dirichlet boundary conditions.

The volume \hat{V} can then be approximated by a truncated spherical Bessel approximation as follows:

$$(56) \quad \hat{V}_a(\rho, \theta, \varphi) = \sum_{l=0}^L \sum_{s=1}^{S(l)} \sum_{m=-l}^l a_{l,m,s} \phi_{l,m,s}(\rho, \theta, \varphi).$$

Here, $a_{l,m,s} \in \mathbb{C}$ are suitable expansion coefficients, $L > 0$ is the truncation limit, and $S(l)$ corresponds to the truncation limit in the radial function for each value of l . In practice, we are given discretized projection samples of \hat{V} and are only able to determine a limited number of coefficients. Specifically, we use the criterion proposed in [12] that determines a truncation limit $S(l)$ as the largest integer s satisfying

$$(57) \quad \frac{z_{l,s+1}}{\pi} \leq A,$$

where $A > 0$ denotes the radius of a ball containing the images. Therefore, the number of coefficients used to represent the volume satisfies $|\mathcal{S}_V| = O\left(\sum_{l=0}^L S(l)(2l+1)\right)$. Typically $S(l) = O(l)$, so we can conclude that $|\mathcal{S}_V| = O(L^3)$.

We also approximate the rotational density using a smooth orthonormal basis, namely the Wigner D-matrices $D_{u,v}^p(R)$ for $p \geq 0$ and $-p \leq u, v \leq p$. For each p , the $(2p+1) \times (2p+1)$ matrix $(D_{u,v}^p(R))_{u,v=-p}^p$ is orthonormal with the (u, v) -th entry given by

$$(58) \quad D_{u,v}^p(R) = e^{-iu\alpha} d_{u,v}^p(\beta) e^{-iv\gamma},$$

where α, β, γ are the Euler angles of R and $d_{u,v}^p$ denotes the (small) Wigner d-matrices [18, p 341]. They are orthogonal to each other and can be used to form an orthonormal basis of $\mathcal{SO}(3)$. In this paper, we only consider densities that are invariant to in-plane rotations, as introduced in Section 3.2.1. For in-plane rotation invariant densities, only coefficients with $v = 0$ are non-vanishing [59]. Therefore, with these assumptions, the rotational density can be represented by

$$(59) \quad \mu_b(R) = \sum_{p=0}^P \sum_{u=-p}^p b_{p,u} D_{u,0}^p(R)$$

where $b_{p,u} \in \mathbb{C}$ are the expansion coefficients. Under this choice, the number of coefficients to represent the rotational density satisfies $|\mathcal{S}_\mu| = O\left(\sum_{p=0}^P (2p+1)\right) = O(P^2)$.

In fact, the entries $D_{u,0}^p(R)$ are proportional to spherical harmonics and are given by

$$(60) \quad D_{u,0}^p(R) = \sqrt{\frac{4\pi}{2p+1}} Y_p^{u*}(\beta, \alpha),$$

where (α, β, γ) is the Euler angle representation of $R \in \mathcal{SO}(3)$. Given (60), the rotational distribution is governed by a probability distribution over \mathbb{S}^2 , which we refer to as the *viewing direction distribution*. Denoting the spherical harmonic basis by

$$(61) \quad \zeta_{p,u}(\alpha, \beta) = 2\pi \sqrt{\frac{4\pi}{2p+1}} Y_p^{u*}(\beta, \alpha),$$

we represent the viewing direction density ν_b as:

$$(62) \quad \nu_b(\alpha, \beta) = \sum_{p=0}^P \sum_{u=-p}^p b_{p,u} \zeta_{p,u}(\alpha, \beta).$$

Consequently, we can factorize the rotational density function into the product of a spherical density and an uniform in-plane density, given by

$$(63) \quad \mu_b(R(\alpha, \beta, \gamma)) = \frac{1}{2\pi} \nu_b(\alpha, \beta)$$

since the uniform in-plane density is $\frac{1}{2\pi}$ for all $\gamma \in [0, 2\pi]$.

The representation of viewing direction density can be further simplified by assuming invariance to in-plane reflection. This can be realized by enforcing the spherical harmonic coefficients of odd degree in (62) to zero, i.e., $b_{p,u} = 0$ if p is odd [75]. In this paper, we only assume the invariance to in-plane rotations but our method can be easily modified to accommodate the additional assumption.

With this choice of basis functions, we can exactly obtain

$$(64) \quad (a, b) \mapsto (\mathcal{M}_c^{(1)}[a, b](\Xi), \mathcal{M}_c^{(2)}[a, b](\Xi^{\otimes 2}), \mathcal{M}_c^{(3)}[a, b](\Xi^{\otimes 3}))$$

using numerical quadrature. Methods for constructing numerical quadrature on $\mathcal{SO}(3)$ or \mathbb{S}^2 can be found in [31, 30], or in Appendix B.

Remark. *Our method is not limited to the basis functions chosen in Section 3.3.1. It can be easily extended to other basis functions. For example, 3-D prolate spheroidal wave functions (3-D PSWF) [32, 44] can also be used to model bandlimited volumes. Other functions suitable for representing molecules include wavelets [19, 73, 9], Gaussian mixtures [37, 15, 81, 17, 16, 41, 40], and neural networks [79, 80, 42, 22, 29]. The basis for rotational density functions can for instance also be chosen as a mixture of von Mises–Fisher distributions [56], or a mixture of point masses on \mathbb{S}^2 [42].*

3.3.2. *Constraints for numerical optimizations.* In this section, we list several necessary constraints to ensure that the solution to the subspace MoM problem (37) provides a valid reconstruction. Firstly, ensuring that the reconstructed volume (the inverse Fourier transform of \hat{V}_a) is a real-valued function is equivalent to requiring that the coefficients satisfy:

$$\alpha_{l,m,s}^*(-1)^m = \alpha_{l,-m,s}(-1)^l.$$

This condition can be enforced by the following re-parameterization:

$$(65) \quad \alpha_{l,m,s} = \begin{cases} \alpha_{l,m,s} - (-1)^{l+m} i \alpha_{l,s,-m}, & m > 0, \\ i^l \alpha_{l,m,s}, & m = 0, \\ i \alpha_{l,m,s} + (-1)^{l+m} \alpha_{l,s,-m}, & m < 0, \end{cases}$$

for $\alpha_{l,m,s} \in \mathbb{R}$.

Secondly, to ensure that the reconstructed viewing direction density is real-valued, we require that

$$b_{p,u} = (-1)^u b_{p,-u}^*.$$

This condition can be enforced by the re-parameterization:

$$(66) \quad b_{p,u} = \begin{cases} \beta_{p,u} + (-1)^u i \beta_{p,-u}, & p > 0, \\ \beta_{0,0}, & p = 0, \\ -i \beta_{p,u} + (-1)^u \beta_{p,-u}, & p < 0, \end{cases}$$

where $\beta_{p,u} \in \mathbb{R}$. For a discussion and derivation of the constraints in (65) and (66), we refer to [59].

Thirdly, we require that ν_b is a probability density function, satisfying

$$\int_0^\pi \int_0^{2\pi} \nu_b(\alpha, \beta) \sin(\beta) \, d\alpha \, d\beta = 1.$$

Since the spherical harmonics satisfy

$$\int_0^\pi \int_0^{2\pi} Y_p^u(\beta, \alpha) \sin(\beta) \, d\alpha \, d\beta = \begin{cases} \sqrt{4\pi}, & p = 0, u = 0, \\ 0, & \text{otherwise,} \end{cases}$$

we can simply fix $b_{0,0} = 1$ and only solve for the rest of the parameters. Finally, we require the viewing direction density to be non-negative, i.e.

$$\nu_b(\alpha, \beta) = \sum_{p=0}^P \sum_{u=-p}^p b_{p,u} \zeta_{p,u}(\alpha, \beta) \geq 0, \quad \forall \alpha \in [0, 2\pi], \beta \in [0, \pi]$$

and we relax this requirement to a set of linear inequality constraints

$$(67) \quad \sum_{p=0}^P \sum_{u=-p}^p b_{p,u} \zeta_{p,u}(\alpha_i, \beta_i) \geq 0, \quad i = 1, \dots, n$$

where $\{(\alpha_i, \beta_i)\}_{i=1}^n$ represents a set of collocation points on \mathbb{S}^2 .

To enforce reflection invariance, we can further impose

$$(68) \quad b_{p,u} = 0, \quad -p \leq u \leq p, \quad \text{for all odd } p.$$

3.3.3. *Two-stage optimization.* Although the third moment contains rich information and can substantially improve the reconstruction, in practice, we observe that the solution to (37) found by many optimization methods may still get stuck at unwanted local minima. Surprisingly, we observe that using a two-stage optimization routine that first attempts to fit only the first two subspace moments and then tries to match the three subspace moments, performs much better.

The two-stage optimization is carried out in the following order:

- In stage one, we only attempt to match the first two (subspace) moments by solving the partial problem:

$$(69) \quad \min_{a,b} \lambda_1 \|\mathcal{M}_c^{(1)}[a, b](\Xi) - \overline{M}_c^{(1)}\|_F^2 + \lambda_2 \|\mathcal{M}_c^{(2)}[a, b](\Xi^{\otimes 2}) - \overline{M}_c^{(2)}\|_F^2.$$

We initialize the coefficients for the volume using i.i.d. Gaussian entries and the coefficients for the rotational density using the coefficients of a randomly generated non-uniform distribution. The optimization process can be completed quickly without the third subspace moment, but the solution will be sensitive to the initial parameters. Therefore, we rerun the optimization multiple times with different random initial parameters. The validity of using moment distances to measure structural similarity between molecules has been demonstrated in [75]. Therefore we only keep that coefficients achieving the minimal loss and use it as a warm start for the optimization problem in the next stage.

- In stage two, we solve the full problem (37) to match all three subspace moments using the warm start obtained from stage one as initialization. The optimization process with the third subspace moment is slower, but we only need to perform it once. The reconstructed volume obtained at the end of stage two will be the final *ab initio* model.

At both stages, we optimize the objective functions using sequential quadratic programming (SQP). Our method is similar to the approach of *sequential moment matching* in [39], where they study the method of moments for estimating Gaussian mixture models. In their analysis, the estimator obtained by sequential moment matching will approximate the maximum likelihood estimator in the low SNR regime, potentially explaining why this two-stage optimization is helpful.

4. NUMERICAL RESULTS

In this section, we present numerical results that demonstrate the performance of our methods in two different settings. In Section 4.1, we provide examples of reconstructing a smooth volume using analytical subspace moments. In Section 4.2, we reconstruct volumes from subspace moments estimated from simulated noisy 2D projections, emulating the setting of performing *ab initio* modeling in Cryo-EM. The molecule data we use is downloaded from the Electron Microscopy Data Bank (<https://www.ebi.ac.uk/emdb/>). All experiments were conducted using MATLAB 2023b on a machine with 120 GB of memory and 12th Gen Intel(R) Core(TM) i9-12900 CPUs running at 2.40GHz.

To evaluate the reconstruction resolution of our method, an alignment is necessary as the moments are invariant to orthonormal transformations of the volume [75]. The alignment can be done using softwares such as ASPIRE [74] and BOTalign [66]. We compute the *Fourier-Shell correlation* (FSC) between the aligned reconstruction and the (downsampled) ground truth, which is a standard metric for measuring reconstruction resolutions in Cryo-EM. On a shell with radius $\kappa > 0$ and a very small width $\delta\kappa > 0$, i.e., $\{\xi \in \mathbb{R}^3 : \kappa \leq \|\xi\| \leq \kappa + \delta\kappa\}$, the FSC between two Fourier volumes is given by:

$$(70) \quad \text{FSC}(\kappa) = \frac{\sum_{\kappa \leq \|\xi\| \leq \kappa + \delta\kappa} \hat{V}_1(\xi) \hat{V}_2^*(\xi)}{\sqrt{\sum_{\kappa \leq \|\xi\| \leq \kappa + \delta\kappa} |\hat{V}_1(\xi)|^2 \sum_{\kappa \leq \|\xi\| \leq \kappa + \delta\kappa} |\hat{V}_2(\xi)|^2}}.$$

The resolution is determined by the frequency κ at which the FSC drops below a cutoff value, conventionally set to be $\frac{1}{7}$ or $\frac{1}{2}$ [55]. Here, we set the cut-off value to $\frac{1}{2}$, as we are comparing the reconstructed volume with the underlying ground truth volume rather than two independent reconstructed volumes from noisy images.

4.1. Reconstruction from analytical subspace moments. In this section, we apply our method to moments generated using the analytical formulas in (34), (35) and (36), which allows us to evaluate the performance of our approach under ideal conditions. In Section 4.1.1, we show how incorporating the third subspace moment can significantly improve the quality of the reconstruction. In Section 4.1.2, we demonstrate the feasibility of using high truncation limits with inexact quadrature for reconstruction.

4.1.1. Effect of adding the third subspace moments. In this first example, we demonstrate the significant improvement achieved by incorporating the third subspace moment in a simplified setting. We assume that both the volume and the viewing direction density are exactly represented by the bases specified in Section 3.3.1. Additionally, we assume exact access to the first three moments (12), (13), and (14) for reconstruction. To create a smooth ground truth volume, we use EMD-34948, originally consisting of $196 \times 196 \times 196$ voxels, with a physical pixel size of 1.04 Å. For computational efficiency, we downsample the volume to $64 \times 64 \times 64$ and expand it into the spherical Bessel basis with a truncation limit of $L = 5$, resulting in a total of $|\mathcal{S}_V| = 1079$ coefficients. This smooth approximation is used as the ground truth volume in this section. Compared to the original data, it achieves a resolution of 17.49 Å. We generate a ground truth viewing direction density by expanding a known density on \mathbb{S}^2 using the spherical harmonic basis.

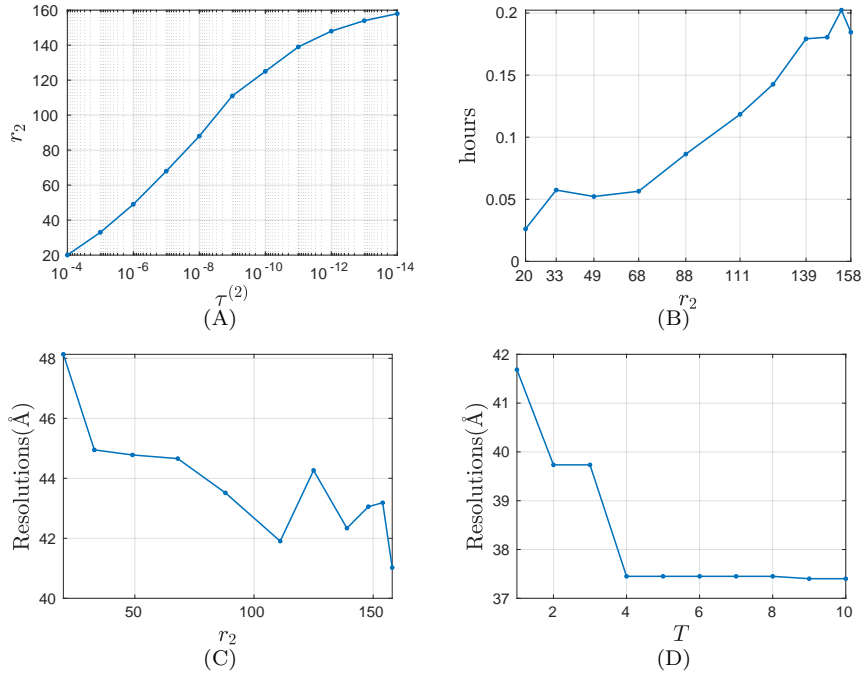


FIGURE 2. (A) The dimension parameter r_2 for the second subspace moment as a function of the threshold value $\tau^{(2)}$ obtained in Section 4.1. Specifically, we obtain $r_2 = 20, 33, 49, 68, 88, 111, 125, 139, 148, 154, 158$. (B) The average running time (in hours) for completing one optimization task (69) as a function of the dimension parameter r_2 , using the values listed above, averaged over 10 re-initializations. (C) The medians of the resolutions obtained from the first two (subspace) moments as a function of r_2 , using the values listed above, based on 10 re-initializations. (D) The resolutions with the first two (subspace) moments as a function of T , where T is the number of re-initializations.

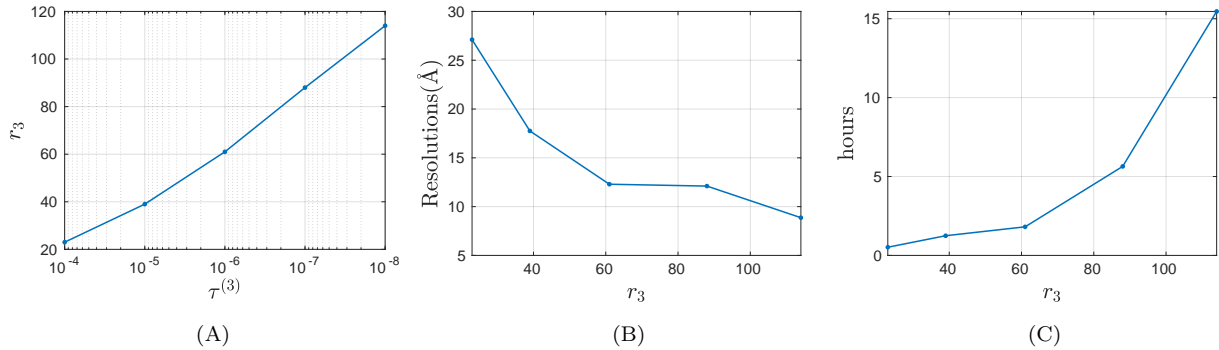


FIGURE 3. (A) The dimension parameter r_3 for the third subspace moment as a function of the threshold value $\tau^{(3)}$ obtained in Section 4.1. (B) The reconstructed resolutions obtained from the first three (subspace) moments as a function of r_3 . (C) The running time (in hours) of solving the optimization problem (37) as a function of r_3 .

Specifically, we use a mixture of 12 von-Mises Fisher distributions (see Appendix C for a brief introduction), with randomly generated centers, equal weights, and a concentration parameter of 4. The mixture density is expanded with a truncation limit of $P = 4$, and the expanded function is re-normalized to form a valid density on \mathbb{S}^2 . The re-normalized function is then symmetrized to create a ground truth density invariant under in-plane reflection, containing $|\mathcal{S}_\mu| = 14$ unknowns. The visualizations of the ground truth volume and

viewing direction density can be found later in Figure 4B and Figure 5A, respectively. With the truncation limits L and P , forming the first three moments with 12-digit accuracy requires 192, 729 and 2080 Gaussian quadrature nodes, respectively. These numbers of nodes are used in this example.

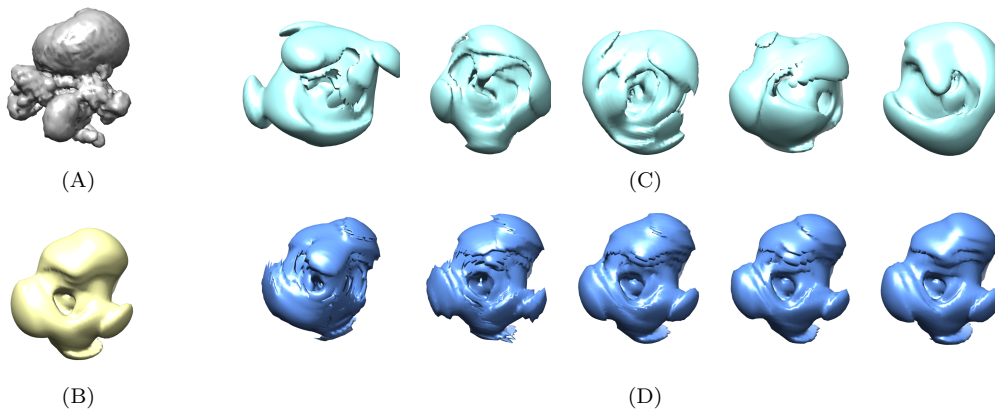


FIGURE 4. (A) The gray volume represents the original EMD-34948 data, downsampled to $64 \times 64 \times 64$. (B) The yellow volume is the smooth approximation of EMD-34948, obtained by expansion into the spherical Bessel basis with $L = 5$, used as the ground truth volume in Section 4.1. (C) The sky-blue volumes (from left to right) represent reconstructions with second subspace moment dimensions $r_2 = 0, 68, 88, 125, 158$. (D) The cornflower-blue volumes (from left to right) represent reconstructions with third subspace moment dimensions $r_3 = 0, 23, 39, 88, 114$.

We begin by studying the reconstruction performance based on only the first two (subspace) moments. We apply the randomized range finding algorithm to $\mathcal{M}^{(2)}[a_\star, b_\star]$ with an oversampling size $s = 250$. By varying the threshold value $\tau^{(2)} = 10^{-4}, 10^{-7}, \dots, 10^{-14}$, we obtain the second subspace moments $\mathcal{M}_{\tau^{(2)}}^{(2)}[a_\star, b_\star] \in \mathbb{C}^{r_2(\tau^{(2)}) \times r_2(\tau^{(2)})}$ where $r_2(\tau^{(2)})$ denotes the dimension parameter obtained at $\tau^{(2)}$. As $\tau^{(2)}$ decreases, the dimension r_2 increases from 20 to 158 as plotted in Figure 2A, and it stops increasing for smaller $\tau^{(2)} < 10^{-14}$. Prior to optimization, we randomly generate 10 initial coefficient vectors, initializing volume coefficients using small i.i.d. mean-zero Gaussian entries and viewing direction coefficients from a randomly generated non-uniform distribution. Using each initial coefficient vector, we solve the stage one optimization problems in (69) with $(\overline{M}_c^{(1)}, \overline{M}_c^{(2)}) = (\mathcal{M}^{(1)}[a_\star, b_\star], \mathcal{M}_{\tau^{(2)}}^{(2)}[a_\star, b_\star])$ for all $\tau^{(2)}$'s. The running time for completing one optimization task is approximately 1.5 minutes when $r_2 = 20$, increasing to about 11 minutes when $r_2 = 158$. Figure 2B illustrates the relationship between the average running time based on the 10 initial parameter vectors and the dimension parameter of the subspace second moment r_2 . We observe that for small r_2 , the optimization problem in stage one (69) is highly sensitive to the initial parameters. As r_2 increases, the reconstructed resolutions show limited improvements, as illustrated in Figure 2C. Some of the reconstructed volumes are visualized in Figure 4C. We further compute the reconstruction error of the coefficients obtained from the first T initial parameter vectors based on the criteria described in Section 3.3.3 as a function of T when $\tau^{(2)} = 10^{-14}$ and $r_2 = 158$, shown in Figure 2D. When $T \geq 4$, the reconstruction error saturates, suggesting that excessive re-initialization does not significantly improve the resolution. In practice, we find $T = 5$ re-initializations balance running time and resolution. For the rest of the experiments in this section, we choose the reconstructed coefficient vector that achieves the smallest objective loss in (69) among the first 5 initial coefficient vectors when $\tau^{(2)} = 10^{-14}$ and $r_2 = 158$, and use it as a warm start for the stage two optimization.

We compress the third moment $\mathcal{M}^{(3)}[a_\star, b_\star]$, using the threshold values $\tau^{(3)} = 10^{-4}, 10^{-5}, \dots, 10^{-8}$, resulting in the third subspace moments $\mathcal{M}_{\tau^{(3)}}^{(3)}[a_\star, b_\star] \in \mathbb{C}^{r_3(\tau^{(3)}) \times r_3(\tau^{(3)}) \times r_3(\tau^{(3)})}$, each associated with a different dimension parameter $r_3(\tau^{(3)})$. As $\tau^{(3)}$ decreases, the dimension parameter r_3 increases from 23 to 114, as shown in Figure 3A. Using the warm start obtained from the first two (subspace) moments, we solve the optimization problem in (37) with $(\overline{M}_c^{(1)}, \overline{M}_c^{(2)}, \overline{M}_c^{(3)}) = (\mathcal{M}^{(1)}[a_\star, b_\star], \mathcal{M}_{\tau^{(2)}}^{(2)}[a_\star, b_\star], \mathcal{M}_{\tau^{(3)}}^{(3)}[a_\star, b_\star])$ for

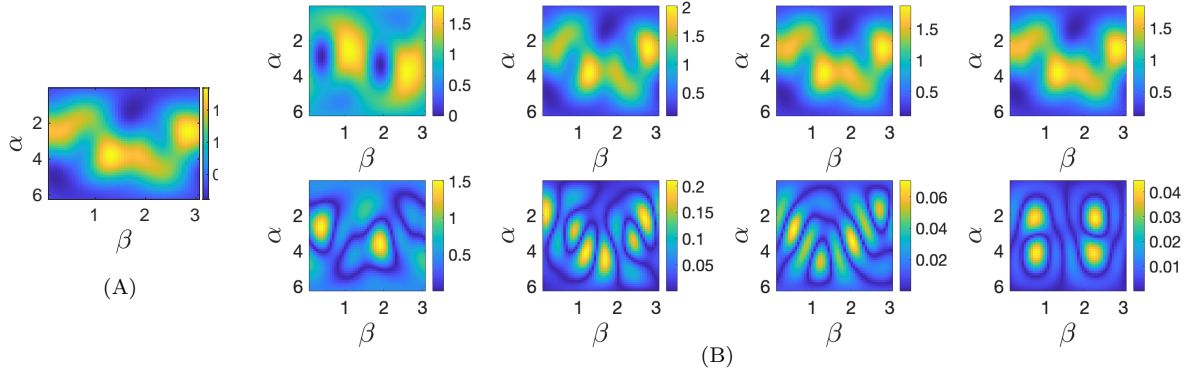


FIGURE 5. (A) The ground truth viewing direction density (as a function of first two Euler angles $\alpha \in [0, 2\pi], \beta \in [0, \pi]$) that is invariant to in-plane reflection. (B) The first row shows the estimated densities with the dimension of the third subspace moments $r_3 = 0, 39, 88, 114$. The second row shows the corresponding absolute point-wise errors compared to the ground truth density. They are also shown as functions of the first two Euler angles.

fixed $\tau^{(2)} = 10^{-14}$ and varying $\tau^{(3)}$'s. The resolution obtained by the warm start is 39.73 \AA , and is improved to 8.87 \AA after stage two optimization when $r_3 = 114$. The relationship between the reconstruction error and the dimension parameter r_3 is displayed in Figure 3B, showing that the reconstructed resolution improves significantly as r_3 increases, with the running time also increases as shown in Figure 3C. The effect of increasing $r^{(3)}$ to the reconstructed volumes and the estimated viewing direction densities along with the estimated errors are visualized in Figure 4 and Figure 5. Despite being less smooth, the reconstructed volume closely approximates the ground truth in shape and the estimated viewing direction density has small errors when r_3 is sufficiently large, suggesting the importance of using the third subspace moment.

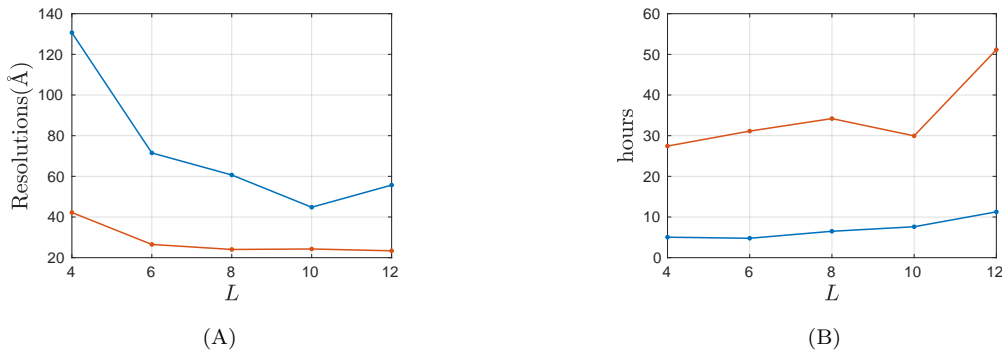


FIGURE 6. (A) The resolutions achieved by the reconstructed volumes at different truncation levels L . The red curve represents the results from stage two, while the blue curve represents those from stage one. (B) The running time (in hours) required to complete the optimization. The red curve corresponds to stage two, and the blue curve corresponds to stage one.

4.1.2. *Effect of truncation limits.* In the next experiment, we use the same ground truth viewing direction distribution as in Section 4.2 and expand the downsampled EMD-34948 data at $L = 12$ as the ground truth volume, achieving a resolution of 9.24 \AA compared to the original data. We compress the analytical moments with the sampling size for randomized sketching being $s = 250$ and threshold parameters $\tau^{(2)} = 10^{-8}, \tau^{(3)} = 10^{-6}$, resulting the subspace moments with $r_2 = 235$ and $r_3 = 128$. The reconstruction algorithms are run with 5 re-initializations, and the estimated density function is expanded at $P = 6$, which contains 28 viewing direction coefficients. For the reconstructed volume, we vary the truncation limits $L = 4, 6, 8, 10, 12$,

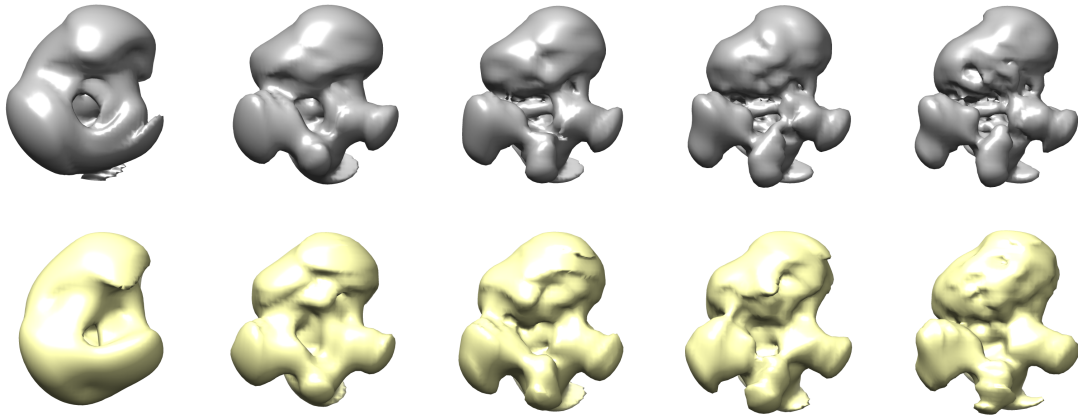


FIGURE 7. The first row shows the expansion of EMD-34948 data into the spherical Bessel basis with truncation limits $L = 4, 6, 8, 10, 12$. The second row shows the reconstructed volumes from the analytical subspace moments of the expanded EMD-34948 at $L = 12$, which are expanded with truncation limits $L = 4, 6, 8, 10, 12$, respectively.

corresponding to 760, 1456, 2352, 3432, 4680 volume coefficients, respectively. We use a quadrature rule with 2184 nodes to integrate all three analytical subspace moments during reconstruction, which is the maximum number of nodes that the memory can accommodate for $L = 12$. The quadrature formula is inexact, incurring a relative error of $O(10^{-3})$ for the second analytical subspace moment at $L = 8, 10, 12$ and for the third analytical subspace moment when $L = 6, 8, 10, 12$.

The resolutions and running times are shown in Figure 6. We observe that the resolution improves as the truncation limit L increases, with the optimal resolution reaching approximately 23.38 \AA at $L = 12$. The running time also increases significantly, as the number of optimized parameters grows as $O(L^3)$. When $L = 12$, the stage one optimization takes 11.26 hours and the stage two optimization takes 51.14 hours. Considering time complexity, the optimal truncation limit would be $L = 8$ or 10 . In Figure 7, we visualize the final reconstructed volumes and the expansions of the original data into the spherical Bessel basis for different truncation limits L . During visualization, we apply Gaussian masks to all reconstructed volumes, with the width of the Gaussian set to the unit length of a pixel. This has small impact on the resolution but significantly improves the visualization quality. We observe that our method provides a reasonable approximation to the ground truth for sufficiently large values of L .

4.2. Reconstruction from noisy images. In this section, we compute the estimated subspace moments from synthetic noisy datasets and apply our reconstruction algorithms using these estimates. The original EMD-34948 data serves as the ground truth volume. For the ground truth viewing direction distribution, we use the mixture of von Mises-Fisher distributions, which is used to generate the ground truth in Section 4.1, as illustrated in Figure 8A. To form the estimated subspace moments, we generate images of varying sample sizes, $N = 10^4, 10^5$ and 10^6 . We vary the signal-to-noise ratio (SNR) with values $\text{SNR} = 1, 0.1$ and 0.01 , resulting in 9 different sets of subspace moments. Here, the SNR in the image I is defined as $\|I - \epsilon\|_F^2 / \|\epsilon\|_F^2$ where ϵ denotes the 2-D Gaussian noise. The effect of the three SNR levels is displayed in Figure 8B. Here, the images are generated to be perfectly centered and are not affected by a contrast transfer function (CTF). Including these effects may further deteriorate the quality of the reconstructions in practice.

During the formation, we symmetrize the moments using the method discussed in Section 3.2.1. Specifically, for each generated image, we create four additional rotated copies with rotation angles $\frac{1}{5} \cdot 2\pi, \frac{2}{5} \cdot 2\pi, \frac{3}{5} \cdot 2\pi, \frac{4}{5} \cdot 2\pi$. Including the original image, we also compute their reflected copies, resulting in nine additional images that are incorporated into the moment formation. The images are downsampled to a size of 64×64 for computational efficiency. We perform the debiasing procedure during the process, with details provided in Appendix A. To determine the size of the subspace moments, we use the method outlined in Section 3.2, applying threshold parameters $\tau^{(2)} = 10^{-8}, \tau^{(3)} = 10^{-6}$ for the case ($N = 10^4, \text{SNR} = 1$), which yields $r_2 = 246$ and $r_3 = 102$. For other values of N and SNR, we use the same subspace moment sizes as in the

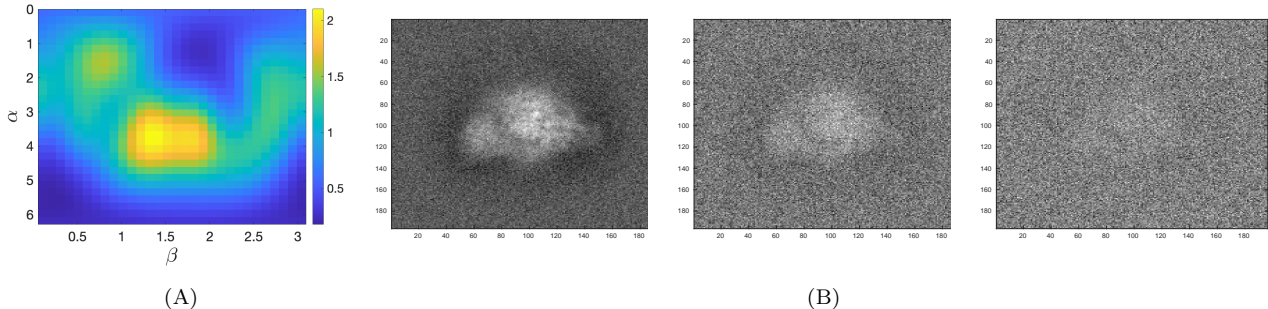


FIGURE 8. (A) The ground truth viewing direction density as a function of the first two Euler angles used in Section 4.2. (B) Noisy projections of EMD-34948 with SNR = 1, 0.1, 0.01, respectively.

case ($N = 10^4$, SNR = 1) for consistent comparison in future analysis. The time required for the formation process is proportional to the original sample size N , with approximately 0.4, 4 and 40 hours needed for $N = 10^4, 10^5$ and 10^6 , respectively, excluding the time for generating raw images.

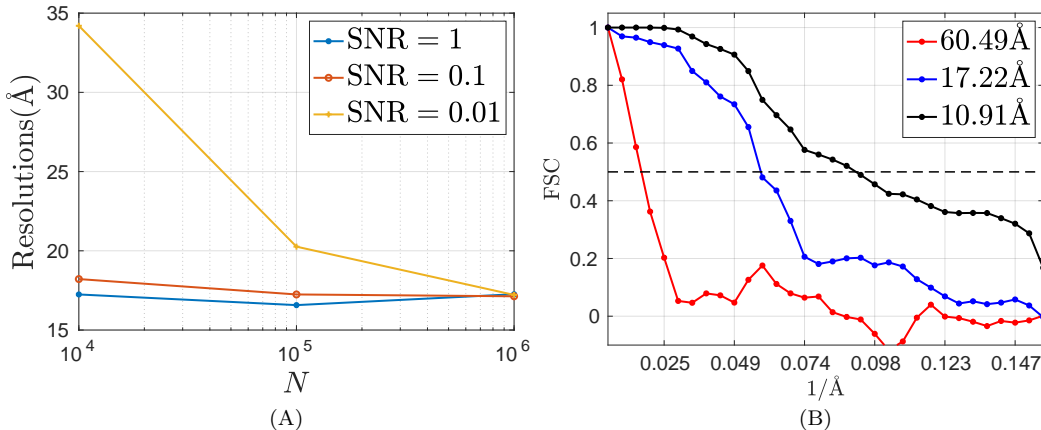


FIGURE 9. (A) The final reconstructed resolutions with the estimated subspace moments generated with different sample sizes N and SNR's. (B) The FSC curves of the reconstructed volumes for $N = 10^6$ and SNR = 0.01. The red curve corresponds to the reconstructed volume using the first two estimated subspace moments, while the blue curve corresponds to the reconstructed volume using all three estimated subspace moments, both expanded at $L = 10$. Additionally, the FSC curve of the expanded volume at $L = 10$ is shown in black.

For the reconstruction step, we expand the volume with $L = 10$ and the density with $P = 6$, which contains $|S_V| = 3432$ coefficients for volume and $|S_\mu| = 28$ coefficients for viewing direction density. We use a quadrature rule with 2496 nodes, which is the maximum number of nodes that the memory can accommodate for the existing parameters. Although the ground truth viewing direction distribution is not invariant to in-plane reflection, we have included that symmetry into the estimated subspace moments. Therefore we need to enforce the estimated viewing distribution to have the symmetry via (68). The precomputation step takes about 40 minutes. It takes 6 to 9 hours to complete the stage one optimization, and 14 to 19 hours to complete the stage two optimization, with the average total running time 22 hours to complete the two-stage optimization step. Our current implementation does not support parallelization, but this could be integrated in future work. For instance, the sketching of images could be parallelized across multiple streams, and the loss and gradient evaluations, involving iterations over different quadrature nodes, could also be executed in parallel. Those will speed up the method significantly.

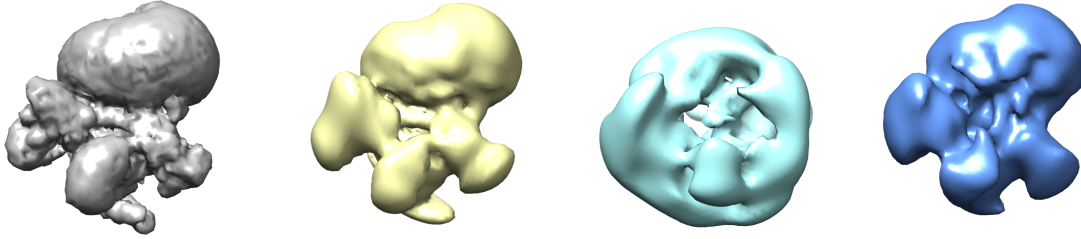


FIGURE 10. From left to right: the ground truth volume, the expanded volume, the reconstructed volume using the first two estimated subspace moments, and the reconstructed volume using all three estimated subspace moments for $N = 10^6$ and $\text{SNR} = 0.01$.

Due to various sources of noise, the reconstructed volumes from the optimization results are non-smooth and contain artifacts, which requires postprocessing. Before applying the Gaussian mask, we zero out entries in the reconstructions outside a specified radius, which is set to 0.6 times the image radius. In practice, we can estimate this radius from denoised images [46]. Then, we compare the final reconstructed volumes with the ground truth volume by computing their FSCs. The resolutions obtained from the first two moments exhibit large variances, ranging from 52.13 Å to 153.26 Å. In contrast, the resolutions obtained from all three moments are significantly improved and display reasonable relationships with N and SNR, as shown in Figure 9A. Even in the worst scenario ($N = 10^4$, $\text{SNR} = 0.01$), the resolution obtained from all three moments is 34.20 Å, which is still better than the best resolution achieved with only the first two moments. When the sample size is sufficiently large ($N = 10^6$), the final reconstructed resolution is around 17.20 Å for all SNR's, demonstrating the robustness of the MoM approach to noise. We obtain a better result than that in Section 4.1.2, as a more accurate quadrature rule is used. For comparison, the direct expansion of the original data into the spherical Bessel basis with $L = 10$ achieves a resolution of 10.90 Å. The FSC curves for the reconstructed volumes with $N = 10^6$, $\text{SNR} = 0.01$ are shown in Figure 9B, with visual comparisons of the volumes provided in Figure 10. These results clearly demonstrate that using only the first two moments provides a crude estimate, while incorporating the third moment yields a much more accurate approximation to the ground truth, capturing nearly all of the main features. Although we are not directly estimating the ground truth viewing direction density, our estimate is expected to approximate its symmetrized version. To obtain a reference viewing direction density, we expand the ground truth with $P = 6$, and enforce symmetry via (68). Figure 11 visualizes the reference density, the estimated density for $N = 10^6$, $\text{SNR} = 0.01$ and the error plot. The estimated density also gives a reasonable approximation to the reference density. As a result, both the reconstructed volume and the estimated density can be used to initialize iterative refinements.

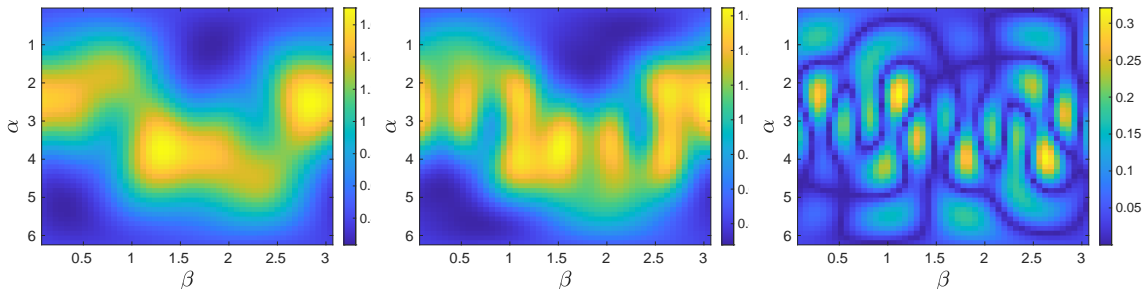


FIGURE 11. From left to right: the reference viewing direction density obtained by expanding and symmetrizing the ground truth, the estimated viewing direction density for $N = 10^6$ and $\text{SNR} = 0.01$, and their absolute point-wise differences. They are shown as functions of the first two Euler angles.

We have not compared our results with other *ab initio* methods such as common-lines based methods [63] because these methods may fail at low SNR, while the MoM approach still provides reasonable resolution,

as long as enough image samples are provided. The reconstructed volumes from the first three (subspace) moments provide a reasonable approximation to the ground truth volumes, indicating that incorporating higher-order moments can be practically useful for the method of moments based approach.

5. DISCUSSION

In this paper, we presented a modular and scalable approach to implementing the method of moments (MoM) in Cryo-EM using the first three moments. To achieve computational efficiency, we applied subspace projections to compress the moments and used a streaming strategy to perform projection and randomized sketching with reduced complexity. Additionally, we discretized the compressed representation using (inexact) numerical quadrature, for additionally reduced complexity. Our numerical results on synthetic datasets used a two-stage optimization routine and produced good *ab initio* models using the first three subspace moments under a non-uniform viewing direction distribution. Future work will validate our computational approach also on experimentally obtained datasets. We expect this to be possible due to recent improvements to particle centering [36] and techniques dealing with the aberrations introduced by contrast transfer functions [46]. Additionally, it would be an interesting problem to apply the techniques of this article to approaches that form higher-order moments of entire micrographs and therefore sidestep particle picking [7].

Our computational pipeline is quite flexible and allows for several natural extensions. One direct extension is to compress moments with higher order moments than the third moment. Additionally, other forms of tensor representation can be used to form a compressed representation of higher-order moments [49]. In this paper, we approximate the volume and rotational density in suitable smooth bases. Other bases such as wavelets may be able to handle more intricate biological molecules. Enforcing sparsity of the volume during reconstruction has been demonstrated to be very effective when using the second moment [9], and can also be included in our framework. Furthermore, molecular priors [28] based on Wilson statistics, i.e., asymptotic properties of the power spectrum of biological molecules [65], could be used to improve the condition number of the optimization by re-weighting the moments. There are also some further numerical questions to be studied, such as devising criteria for choosing weights in the optimization problem (37) and choosing quadrature rules that balance the quadrature errors and the computational cost. These questions will be studied in future work.

Our results demonstrate that the method of moments can yield reasonable *ab initio* models, even for small molecules and low SNR. This is a setting where state-of-the-art tools [57, 51] encounter difficulties, although particle picking can be performed [72, figure 10 f-h] and the method of moments therefore can be employed.

ACKNOWLEDGEMENT

Y. Khoo was supported by DMS-2111563, DMS-2339439 and DE-SC0022232. A. Singer and O. Mickelin were supported in part by AFOSR FA9550-20-1-0266 and FA9550-23-1-0249, the Simons Foundation Math+X Investigator Award, NSF DMS 2009753, and NIH/NIGMS R01GM136780-01. Y. Wang is supported with funding by the University of Chicago Data Science Institute (DSI).

Y. Wang has used ChatGPT to edit and polish the written text for spelling and grammar. Y. Wang would like to thank Fengyu Yang and Chugang Yi for many helpful discussions during the initial stages of the project.

APPENDIX A. DEBIASING THE EMPIRICAL (SUBSPACE) MOMENTS

In this appendix, we provide the details of our debiasing procedure. We assume the noisy pre-processed Fourier images are generated from a ground truth structure (V_\star, μ_\star) by

$$(71) \quad \hat{I}_j = H(\mathcal{I}[V_\star, R_j] + \epsilon_j), \quad \epsilon_j \stackrel{i.i.d.}{\sim} \mathcal{N}(0, \sigma^2 I_D), \quad R_j \stackrel{i.i.d.}{\sim} \mu_\star \quad j = 1, \dots, N$$

where N is the number of noisy images and D is the dimension of the image in its vectorized form. Here we let $H \in \mathbb{C}^{d \times D}$ be the composition of two known transforms given by $H = \mathcal{S}\mathcal{F}$ where $\mathcal{F} \in \mathbb{C}^{D \times D}$ is the 2-D discrete Fourier transform matrix and $\mathcal{S} \in \mathbb{C}^{d \times D}$ is the downsampling operator. The positive integer d denotes the dimension of the downsampled images. For simplicity, we denote the pre-processed clean projection by $\hat{I}_{R_j} = H\mathcal{I}[V_\star, R_j]$.

When N is sufficiently large, the empirical first moment is an unbiased estimator since

$$\begin{aligned}\tilde{M}^{(1)} &= N^{-1} \sum_{j=1}^N I_j = N^{-1} \sum_{j=1}^N \hat{I}_{R_j} + N^{-1} \sum_{j=1}^N H\epsilon_j \\ &\xrightarrow{N \rightarrow \infty} \mathbb{E}_{R \sim \mu_*} [I_R] + H\mathbb{E}[\epsilon] = M^{(1)}.\end{aligned}$$

Consequently, we set the estimated first moment $\overline{M}^{(1)} = \tilde{M}^{(1)}$.

The empirical second moment is calculated as

$$\begin{aligned}\tilde{M}^{(2)} &= N^{-1} \sum_{j=1}^N \hat{I}_{R_j} \hat{I}_{R_j}^T + N^{-1} \sum_{j=1}^N \hat{I}_{R_j} (H\epsilon_j)^* + N^{-1} \sum_{j=1}^N (H\epsilon_j) \hat{I}_{R_j}^* + N^{-1} \sum_{j=1}^N (H\epsilon_j)(H\epsilon_j)^* \\ &\xrightarrow{N \rightarrow \infty} \mathbb{E}_{R \sim \mu_*} [\hat{I}_R \hat{I}_R^T] + 2\mathbb{E}_{R \sim \mu_*} [\hat{I}_R] H\mathbb{E}[\epsilon] + H\mathbb{E}[\epsilon \epsilon^*] H^* = M^{(2)} + \sigma^2 H H^*.\end{aligned}$$

Hence, the bias on $\tilde{M}^{(2)}$ is

$$(72) \quad B^{(2)} = \sigma^2 \mathcal{S} \mathcal{F} (\mathcal{S} \mathcal{F})^* = \sigma^2 \mathcal{S} \mathcal{F} \mathcal{F}^* \mathcal{S}^* = \sigma^2 \mathcal{S} \mathcal{S}^* = \sigma^2 I_d.$$

where we have used the facts that the 2-D Fourier transform is unitary and the low-pass filter satisfies $\mathcal{S} \mathcal{S}^* = \mathcal{S} \mathcal{S}^T = I_d$, which can be easily verified.

The empirical third moment is calculated as

$$\begin{aligned}\tilde{M}^{(3)} &= N^{-1} \sum_{j=1}^N \left(\hat{I}_{R_j} \right)^{\otimes 3} \\ &+ N^{-1} \sum_{j=1}^N \hat{I}_{R_j} \otimes (H\epsilon_j) \otimes (H\epsilon_j) + N^{-1} \sum_{j=1}^N (H\epsilon_j) \otimes \hat{I}_{R_j} \otimes (H\epsilon_j) + N^{-1} \sum_{j=1}^N (H\epsilon_j) \otimes (H\epsilon_j) \otimes \hat{I}_{R_j} \\ &+ N^{-1} \sum_{j=1}^N \hat{I}_{R_j} \otimes \hat{I}_{R_j} \otimes (H\epsilon_j) + N^{-1} \sum_{j=1}^N (H\epsilon_j) \otimes \hat{I}_{R_j} \otimes \hat{I}_{R_j} + N^{-1} \sum_{j=1}^N \hat{I}_{R_j} \otimes (H\epsilon_j) \otimes \hat{I}_{R_j} \\ &\quad \underbrace{\hspace{15em}}_{\rightarrow 0, \text{ as } N \rightarrow \infty} \\ &\xrightarrow{N \rightarrow \infty} M^{(3)} + \mathbb{E}[M^{(1)} \otimes (H\epsilon) \otimes (H\epsilon)] + \mathbb{E}[(H\epsilon) \otimes M^{(1)} \otimes (H\epsilon)] + \mathbb{E}[(H\epsilon) \otimes (H\epsilon) \otimes M^{(1)}].\end{aligned}$$

We can represent the noise vector as $\epsilon = \sum_{i=1}^D \xi_i e_i$ where $\xi_i \stackrel{i.i.d.}{\sim} \mathcal{N}(0, \sigma^2)$ and e_i is the i -th elementary basis vector in \mathbb{R}^D . Then we have

$$\begin{aligned}\mathbb{E}[M^{(1)} \otimes (H\epsilon) \otimes (H\epsilon)] &= \left(\sum_{i,j=1}^D \mathbb{E}[\xi_i \xi_j] (M^{(1)} \otimes e_i \otimes e_j) \right) \times_1 I_d \times_2 H \times_3 H \\ &= \left(\sum_{i,j=1}^D \sigma^2 \delta_{i=j} (M^{(1)} \otimes e_i \otimes e_j) \right) \times_1 I_d \times_2 H \times_3 H \\ &= \sigma^2 \sum_{i=1}^D (M^{(1)} \otimes (H_i) \otimes (H_i)),\end{aligned}$$

and similar results hold for $\mathbb{E}[(H\epsilon) \otimes M^{(1)} \otimes (H\epsilon)]$ and $\mathbb{E}[(H\epsilon) \otimes (H\epsilon) \otimes M^{(1)}]$. Combining them all together, we get

$$(73) \quad B^{(3)} = \sigma^2 \sum_{i=1}^D \left(M^{(1)} \otimes H_i \otimes H_i + H_i \otimes M^{(1)} \otimes H_i + H_i \otimes H_i \otimes M^{(1)} \right).$$

Therefore, we can obtain the estimated second and third moments by debiasing the empirical second and third moments via

$$\begin{aligned}\overline{M}^{(2)} &= \tilde{M}^{(2)} - B^{(2)}, \\ \overline{M}^{(3)} &= \tilde{M}^{(3)} - B^{(3)}.\end{aligned}$$

When performing sketching, we also sketch the biases $B^{(2)}, B^{(3)}$ and subtract them from the sketched empirical moments on the fly, through

$$\begin{aligned}B^{(2)}G &= \sigma^2 G \\ \mathcal{S}[G^{(1)}, G^{(2)}](B^{(3)}) &= \sigma^2 \sum_{i=1}^D (\overline{M}^{(1)} \otimes [((G^{(1)})^T H_i) \odot ((G^{(2)})^T H_i)]^T \\ &\quad + H_i \otimes [((G^{(1)})^T \overline{M}^{(1)}) \odot ((G^{(2)})^T H_i)]^T + H_i \otimes [((G^{(1)})^T H_i) \odot ((G^{(2)})^T \overline{M}^{(1)})]^T)\end{aligned}$$

where $G \in \mathbb{R}^{d \times r_2}$, $G^{(1)}, G^{(2)} \in \mathbb{R}^{d \times r_3}$ are independent random Gaussian matrices and $\mathcal{S}[G^{(1)}, G^{(2)}] : \mathbb{R}^{d \times d \times d} \rightarrow \mathbb{R}^{d \times r_3}$ is the structured tensor sketch operator defined in (46). When forming the estimated subspace moments, we compress the biases using the obtained matrices $U^{(k)}$ for $k = 2, 3$ and subtract them on the fly, which can be done in a similar way. We omit the details here.

APPENDIX B. QUADRATURE RULES FOR SUBSPACE MOMENTS

In this section, we introduce the Euler angle parameterization of 3-D rotations used in this paper. We can represent any rotation matrix $R \in \mathcal{SO}(3)$ by the product of three elementary rotation matrices given by

$$R = R_z(\alpha)R_y(\beta)R_z(\gamma).$$

Here, $\alpha \in [0, 2\pi]$, $\beta \in [0, \pi]$ and $\gamma \in [0, 2\pi]$ are the Euler angles under the ZYZ convention, and R_z, R_y are the elementary rotation matrices defined as

$$R_y(\theta) = \begin{pmatrix} \cos \theta & 0 & \sin \theta \\ 0 & 1 & 0 \\ -\sin \theta & 0 & \cos \theta \end{pmatrix}, \quad R_z(\phi) = \begin{pmatrix} \cos \phi & -\sin \phi & 0 \\ \sin \phi & \cos \phi & 0 \\ 0 & 0 & 1 \end{pmatrix}.$$

The Haar integral of any function f over $\mathcal{SO}(3)$ can be defined as

$$(74) \quad \int_{\mathcal{SO}(3)} f(R) dR = \frac{1}{8\pi^2} \int_0^{2\pi} \int_0^\pi \int_0^{2\pi} f(R(\alpha, \beta, \gamma)) d\alpha \sin \beta d\beta d\gamma.$$

We assume that the function f can be expanded by Wigner D-matrices (58) with a truncation limit L . To evaluate the integral in (74), we want to find a quadrature rule that can integrate all the entries of the Wigner D-matrices

$$\left\{ D_{m,m'}^l(R) \mid 0 \leq l \leq L, -l \leq m, m' \leq l \right\}$$

with respect to the Haar measure. A particular choice is given by the Lemma 3.1 in [31] for constructing such a rule, which is formed by the product of two quadrature rules. The first rule can integrate the spherical harmonics with truncation limit L :

$$\left\{ Y_l^m(\beta, \alpha) \mid 0 \leq l \leq L, -l \leq m \leq l \right\}.$$

with respect to the spherical measure $d\alpha \sin \beta d\beta$ over $[0, 2\pi] \times [0, \pi]$. For this one, we use the Gaussian quadrature rules over \mathbb{S}^2 constructed in [31, 30], which guarantee 12 digits of accuracy. They are generously provided to download from the website via the link. The second quadrature rule can integrate the 1-D Fourier basis

$$\left\{ e^{im\gamma} \mid -L \leq m \leq L \right\}$$

with respect to $d\gamma$ over $[0, 2\pi]$. We use a trapezoidal rule on $[0, 2\pi]$ with $L+1$ equispaced quadrature points.

When the volume and the rotational density are represented by the spherical Bessel basis and the Wigner D-matrices respectively, the moments can be fully represented by the Wigner D-matrices. Therefore,

	$P = 2$	$P = 3$	$P = 4$	$P = 5$
$L = 4$	(90, 378, 926)	(110, 432, 1066)	(140, 522, 1274)	(160, 576, 1352)
$L = 5$	(132, 638, 1664)	(168, 704, 1952)	(192, 792, 2080)	(252, 902, 2368)
$L = 6$	(196, 936, 2812)	(224, 1066, 2964)	(294, 1274, 3382)	(336, 1352, 3534)
$L = 7$	(256, 1470, 4092)	(336, 1560, 4620)	(384, 1830, 4840)	(464, 1950, 5368)
$L = 8$	(378, 2074, 6100)	(432, 2210, 6350)	(522, 2516, 7050)	(576, 2652, 7300)
$L = 9$	(480, 2812, 8176)	(580, 2964, 9016)	(640, 3382, 10192)	(720, 3534, 10192)
$L = 10$	(638, 3738, 11284)	(704, 3906, 12710)	(792, 4410, 12710)	(902, 4620, 13082)
$L = 11$	(768, 4830, 14348)	(864, 5060, 15572)	(984, 5612, 16048)	(1176, 5842, 17272)
$L = 12$	(936, 6100, 18796)	(1066, 6350, 19314)	(1274, 7050, 24864)	(1352, 7300, 24864)

TABLE 1. The sizes of the constructed quadrature rules, which can form the first three (subspace) moments with 12 digits of accuracy when the volume is represented by the spherical Bessel basis with a truncation limit of L and the rotational density is represented by the Wigner-D matrices with a truncation limit of P . The Gaussian quadrature that can integrate the spherical harmonics with order 31 is not provided on the website. Hence in the code, we use the Gaussian quadrature for 32 as a replacement.

the constructed quadrature rules in this Appendix can be applied to integrate the moments with machine precision. To see this, we use the fact that the representation of rotating the spherical harmonic Y_l^m by $R^{-1} \in \mathcal{SO}(3)$ is given by the Wigner-D matrix $(D_{m,m'}^l(R))_{m,m'=-l}^l$, through

$$(75) \quad (R^{-1} \circ Y_l^m)(\theta, \varphi) = \sum_{m'=-l}^l \overline{D_{m,m'}^l(R)} Y_l^{m'}(\theta, \varphi) = \sum_{m'=-l}^l (-1)^{m-m'} D_{m',m}^l(R) Y_l^{m'}(\theta, \varphi)$$

Using the Fourier-slice theorem (9), the 2-D projection of the Fourier volume is

$$(76) \quad \hat{\mathcal{I}}[a, R](\rho, \varphi) = \sum_{l=0}^L \sum_{s=1}^{S(l)} \sum_{m=-l}^l \sum_{m'=-l}^l a_{l,m,s} c_{l,s} j_l(\rho \frac{z_{l,s}}{1/2}) (-1)^{m-m'} Y_l^{m'}(\pi/2, \varphi) D_{m',m}^l(R).$$

We use another fact that the product of two Wigner D-matrices with orders l and l' can be linearly represented by the Wigner D-matrices with order less than or equal to $l + l'$, through

$$(77) \quad D_{m_1, m_2}^l(R) D_{m'_1, m'_2}^{l'}(R) = \sum_{p=|l-l'|}^{l+l'} \langle l, m_1, l, m'_1 | p, m_1 + m'_1 \rangle \langle l, m_2, l, m'_2 | p, m_2 + m'_2 \rangle D_{m_1+m'_1, m_2+m'_2}^p(R),$$

where $\langle \dots, \dots | \dots \rangle$ denotes the Clebsch-Gordan coefficients [18, p 351]. The first three subspace moments are formed by outer products of terms in the form of (76), multiplied by a rotational density represented by Wigner-D matrices (59). Combing that with (58), we know that they can be represented by the Wigner D-matrices with orders less than or equal to $L + P, 2L + P$ and $3L + P$ respectively. In Table 1, we list the sizes of the constructed quadrature rules used to form the first three moments as functions of some truncation limits L and P , with 12 digits of accuracy.

APPENDIX C. VON MISES–FISHER DISTRIBUTION

The von Mises–Fisher distribution defined on \mathbb{S}^{d-1} has the probability density function

$$(78) \quad f(x|\mu, \kappa) = C(\kappa) \exp(\kappa \mu^T x),$$

where $\kappa > 0$ is the concentration parameter and the normalizing constant $C(\kappa)$ is given by

$$C(\kappa) = \frac{\kappa^{d/2-1}}{(2\pi)^{d/2} I_{d/2-1}(\kappa)}.$$

Here, I_ν denotes the modified Bessel function of the first kind [14]. In Section 4, we use a mixture of von Mises–Fisher distributions to model the non-uniform viewing direction distribution, whose density is then

given by

$$\rho(x) = \sum_{j=1}^n w_j f(x|\mu_j, \kappa)$$

with $w_j > 0$ and $\sum_{j=1}^n w_j = 1$.

REFERENCES

- [1] Asaf Abas, Tamir Bendory, and Nir Sharon. The generalized method of moments for multi-reference alignment. *IEEE Transactions on Signal Processing*, 70:1377–1388, 2021.
- [2] Emmanuel Abbe, Tamir Bendory, William Leeb, João M. Pereira, Nir Sharon, and Amit Singer. Multireference alignment is easier with an aperiodic translation distribution. *IEEE Transactions on Information Theory*, 65:3565–3584, 2017.
- [3] Thomas Dybdahl Ahle and Jakob Bæk Tejs Knudsen. Almost optimal tensor sketch. *arXiv preprint arXiv:1909.01821*, 2019.
- [4] Philip R. Baldwin and Dmitry Lyumkis. Non-uniformity of projection distributions attenuates resolution in cryo-em. *Progress in Biophysics and Molecular Biology*, 150:160–183, 2020.
- [5] Afonso S. Bandeira, Ben Blum-Smith, Joe Kileel, Jonathan Niles-Weed, Amelia Perry, and Alexander S. Wein. Estimation under group actions: Recovering orbits from invariants. *Applied and Computational Harmonic Analysis*, 66:236–319, 2023.
- [6] Tamir Bendory, Alberto Bartesaghi, and Amit Singer. Single-particle cryo-electron microscopy: Mathematical theory, computational challenges, and opportunities. *IEEE Signal Processing Magazine*, 37(2):58–76, 2020.
- [7] Tamir Bendory, Nicolas Boumal, William Leeb, Eitan Levin, and Amit Singer. Toward single particle reconstruction without particle picking: Breaking the detection limit. *SIAM Journal on Imaging Sciences*, 16(2):886–910, 2023.
- [8] Tamir Bendory and Dan Edidin. The sample complexity of sparse multi-reference alignment and single-particle cryo-electron microscopy. *SIAM Journal on Mathematics of Data Science*, 6(2):254–282, 2024.
- [9] Tamir Bendory, Yuehaw Khoo, Joe Kileel, Oscar Mickelin, and Amit Singer. Autocorrelation analysis for cryo-em with sparsity constraints: Improved sample complexity and projection based algorithms. *Proceedings of the National Academy of Sciences*, 120(18), 2023.
- [10] Tristan Bepler, Andrew Morin, Micah Rapp, Julia Brasch, Lawrence Shapiro, Alex J. Noble, and Bonnie Berger. Positive-unlabeled convolutional neural networks for particle picking in cryo-electron micrographs. *Nature Methods*, 16(11):1153–1160, 11 2019.
- [11] Tejal Bhamre, Teng Zhang, and Amit Singer. Denoising and covariance estimation of single particle cryo-em images. *Journal of Structural Biology*, 195(1):72–81, 2016.
- [12] Tejal Bhamre, Teng Zhang, and Amit Singer. Anisotropic twicing for single particle reconstruction using autocorrelation analysis. *arXiv preprint arXiv:1704.07969*, 2017.
- [13] Ronald N. Bracewell. Numerical transforms. *Science*, 248:697 – 704, 1990.
- [14] Y.A. Brychkov. *Handbook of Special Functions: Derivatives, Integrals, Series and Other Formulas*. CRC Press, 2008.
- [15] Muyuan Chen and Steven J. Ludtke. Deep learning-based mixed-dimensional gaussian mixture model for characterizing variability in cryo-em. *Nature Methods*, 18(8):930–936, 8 2021.
- [16] Muyuan Chen, Michael F. Schmid, and Wah Chiu. Improving resolution and resolvability of single-particle cryoem structures using gaussian mixture models. *Nature Methods*, 21(1):37–40, 1 2024.
- [17] Muyuan Chen, Bogdan Toader, and Roy Lederman. Integrating molecular models into cryoem heterogeneity analysis using scalable high-resolution deep gaussian mixture models. *Journal of Molecular Biology*, 435(9):168014, 2023. New Frontier of Cryo-Electron Microscopy Technology.
- [18] G.S. Chirikjian and A.B. Kyatkin. *Harmonic Analysis for Engineers and Applied Scientists: Updated and Expanded Edition*. Dover Books on Mathematics. Dover Publications, 2016.
- [19] Ingrid Daubechies. *Ten Lectures on Wavelets*. Society for Industrial and Applied Mathematics, 1992.
- [20] Lieven De Lathauwer, Bart De Moor, and Joos Vandewalle. A multilinear singular value decomposition. *SIAM Journal on Matrix Analysis and Applications*, 21(4):1253–1278, 2000.
- [21] Lieven De Lathauwer, Bart De Moor, and Joos Vandewalle. On the best rank-1 and rank- (r_1, r_2, \dots, r_n) approximation of higher-order tensors. *SIAM Journal on Matrix Analysis and Applications*, 21(4):1324–1342, 2000.
- [22] Claire Donnat, Axel Levy, Frédéric Poitevin, Ellen D. Zhong, and Nina Miolane. Deep generative modeling for volume reconstruction in cryo-electron microscopy. *Journal of Structural Biology*, 214(4):107920, 2022.
- [23] Nicha C. Dvornik, Fred J. Sigworth, and Hemant D. Tagare. Subspaceem: A fast maximum-a-posteriori algorithm for cryo-em single particle reconstruction. *Journal of Structural Biology*, 190(2):200–214, 2015.
- [24] Lars Eldén and Berkant Savas. A newton–grassmann method for computing the best multilinear rank- (r_1, r_2, r_3) approximation of a tensor. *SIAM Journal on Matrix Analysis and Applications*, 31(2):248–271, 2009.
- [25] Yifeng Fan and Zhizhen Zhao. Cryo-electron microscopy image denoising using multi-frequency vector diffusion maps. In *2021 IEEE International Conference on Image Processing (ICIP)*, pages 3463–3467, 2021.
- [26] Zhou Fan, Roy R. Lederman, Yi Sun, Tianhao Wang, and Sheng Xu. Maximum likelihood for high-noise group orbit estimation and single-particle cryo-EM. *The Annals of Statistics*, 52(1):52 – 77, 2024.
- [27] Zhou Fan, Yi Sun, Tianhao Wang, and Yihong Wu. Likelihood landscape and maximum likelihood estimation for the discrete orbit recovery model. *Communications on Pure and Applied Mathematics*, 76, 2020.
- [28] Marc Aurèle Gilles and Amit Singer. A molecular prior distribution for bayesian inference based on wilson statistics. *Computer Methods and Programs in Biomedicine*, 221:106830, 2022.

- [29] Nabin Giri, Raj S. Roy, and Jianlin Cheng. Deep learning for reconstructing protein structures from cryo-em density maps: Recent advances and future directions. *Current Opinion in Structural Biology*, 79:102536, 2023.
- [30] Manuel Gräf. Efficient algorithms for the computation of optimal quadrature points on riemannian manifolds. *Chemnitz University of Technology*, 2013.
- [31] Manuel Gräf and Daniel Potts. Sampling sets and quadrature formulae on the rotation group. *Numerical Functional Analysis and Optimization*, 30:665 – 688, 2009.
- [32] Philip Greengard and Kirill Serkh. On generalized prolate spheroidal functions. *arXiv preprint arXiv:1811.02733*, 2018.
- [33] Harshit Gupta, Michael T. McCann, Laurène Donati, and Michael Unser. Cryogan: A new reconstruction paradigm for single-particle cryo-em via deep adversarial learning. *IEEE Transactions on Computational Imaging*, 7:759–774, 2021.
- [34] N. Halko, P. G. Martinsson, and J. A. Tropp. Finding structure with randomness: Probabilistic algorithms for constructing approximate matrix decompositions. *SIAM Review*, 53(2):217–288, 2011.
- [35] Ayelet Heimowitz, Joakim Andén, and Amit Singer. Apple picker: Automatic particle picking, a low-effort cryo-em framework. *Journal of Structural Biology*, 204(2):215–227, 2018.
- [36] Ayelet Heimowitz, Nir Sharon, and Amit Singer. Centering noisy images with application to cryo-em. *SIAM journal on imaging sciences*, 14(2):689–716, 2021.
- [37] Shuai Huang, Mona Zehni, Ivan Dokmanić, and Zhizhen Zhao. Orthogonal matrix retrieval with spatial consensus for 3d unknown view tomography. *SIAM Journal on Imaging Sciences*, 16(3):1398–1439, 2023.
- [38] Zvi Kam. The reconstruction of structure from electron micrographs of randomly oriented particles. *Journal of Theoretical Biology*, 82(1):15–39, 1980.
- [39] Anya Katsevich and Afonso S. Bandeira. Likelihood maximization and moment matching in low snr gaussian mixture models. *Communications on Pure and Applied Mathematics*, 76, 2020.
- [40] Takeshi Kawabata. Multiple subunit fitting into a low-resolution density map of a macromolecular complex using a gaussian mixture model. *Biophysical Journal*, 95(10):4643–4658, 2008.
- [41] Takeshi Kawabata. Gaussian-input gaussian mixture model for representing density maps and atomic models. *Journal of Structural Biology*, 203(1):1–16, 2018.
- [42] Yuehaw Khoo, Sounak Paul, and Nir Sharon. Deep neural-network prior for orbit recovery from method of moments. *Journal of Computational and Applied Mathematics*, 444:115782, 2024.
- [43] Tamara G. Kolda and Brett W. Bader. Tensor decompositions and applications. *SIAM Review*, 51(3):455–500, 2009.
- [44] Roy R. Lederman. Numerical algorithms for the computation of generalized prolate spheroidal functions. *arXiv preprint arXiv:1710.02874*, 2017.
- [45] Eitan Levin, Tamir Bendory, Nicolas Boumal, Joe Kileel, and Amit Singer. 3d ab initio modeling in cryo-em by auto-correlation analysis. In *2018 IEEE 15th International Symposium on Biomedical Imaging (ISBI 2018)*, pages 1569–1573, 2018.
- [46] Nicholas F. Marshall, Oscar Mickelin, Yunpeng Shi, and Amit Singer. Fast principal component analysis for cryo-electron microscopy images. *Biological Imaging*, 3:e2, 2023.
- [47] Nicholas F. Marshall, Oscar Mickelin, and Amit Singer. Fast expansion into harmonics on the disk: A steerable basis with fast radial convolutions. *SIAM Journal on Scientific Computing*, 45(5):A2431–A2457, 2023.
- [48] Joseph A. Mindell and Nikolaus Grigorieff. Accurate determination of local defocus and specimen tilt in electron microscopy. *Journal of Structural Biology*, 142(3):334–347, 2003.
- [49] Ankur Moitra and Alexander S. Wein. Spectral methods from tensor networks. *Symposium on Theory of Computing (STOC)*, 2019.
- [50] Amelia Perry, Jonathan Weed, Afonso S. Bandeira, Philippe Rigollet, and Amit Singer. The sample complexity of multi-reference alignment. *SIAM Journal on Mathematics of Data Science*, 1(3):497–517, 2019.
- [51] Ali Punjani, John L Rubinstein, David J Fleet, and Marcus A Brubaker. cryosparc: algorithms for rapid unsupervised cryo-em structure determination. *Nature methods*, 14(3):290–296, 2017.
- [52] Cyril F. Reboul, Michael Eager, Dominika Elmlund, and Hans Elmlund. Single-particle cryo-em—improved ab initio 3d reconstruction with simple/prime. *Protein Science*, 27, 2018.
- [53] Alexis Rohou and Nikolaus Grigorieff. Ctffind4: Fast and accurate defocus estimation from electron micrographs. *Journal of Structural Biology*, 192(2):216–221, 2015. Recent Advances in Detector Technologies and Applications for Molecular TEM.
- [54] Elad Romanov, Tamir Bendory, and Or Ordentlich. Multi-reference alignment in high dimensions: Sample complexity and phase transition. *SIAM Journal on Mathematics of Data Science*, 3(2):494–523, 2021.
- [55] Peter B Rosenthal and Richard Henderson. Optimal determination of particle orientation, absolute hand, and contrast loss in single-particle electron cryomicroscopy. *Journal of molecular biology*, 333(4):721–745, 2003.
- [56] Fabrice Rossi and Florian Barbaro. Mixture of von mises-fisher distribution with sparse prototypes. *Neurocomputing*, 501:41–74, 2022.
- [57] Sjors H.W. Scheres. Relion: Implementation of a bayesian approach to cryo-em structure determination. *Journal of Structural Biology*, 180(3):519–530, 2012.
- [58] Sjors H.W. Scheres. Semi-automated selection of cryo-em particles in relion-1.3. *Journal of Structural Biology*, 189(2):114–122, 2015.
- [59] Nir Sharon, Joe Kileel, Yuehaw Khoo, Boris Landa, and Amit Singer. Method of moments for 3d single particle ab initio modeling with non-uniform distribution of viewing angles. *Inverse Problems*, 36(4):044003, 2 2020.
- [60] Peter S. Shen. The 2017 nobel prize in chemistry: cryo-em comes of age. *Analytical and Bioanalytical Chemistry*, 410(8):2053–2057, 3 2018.

- [61] Yunpeng Shi and Amit Singer. Ab-initio contrast estimation and denoising of cryo-em images. *Computer Methods and Programs in Biomedicine*, 224:107018, 2022.
- [62] Fred J. Sigworth, Peter C. Doerschuk, Jose-Maria Carazo, and Sjors H.W. Scheres. Chapter ten - an introduction to maximum-likelihood methods in cryo-em. In *Cryo-EM, Part B: 3-D Reconstruction*, volume 482 of *Methods in Enzymology*, pages 263–294. Academic Press, 2010.
- [63] A. Singer and Y. Shkolnisky. Three-dimensional structure determination from common lines in cryo-em by eigenvectors and semidefinite programming. *SIAM Journal on Imaging Sciences*, 4(2):543–572, 2011.
- [64] Amit Singer. Mathematics fro cryo-electron microscopy. *Proceedings of the International Congress of Mathematicians (ICM 2018)*, 2018.
- [65] Amit Singer. Wilson statistics: derivation, generalization and applications to electron cryomicroscopy. *Acta Crystallographica Section A*, 77(5):472–479, 9 2021.
- [66] Amit Singer and Ruiyi Yang. Alignment of density maps in wasserstein distance. *Biological Imaging*, page 1–21, 2024.
- [67] Yiming Sun, Yang Guo, Charlene Luo, Joel Tropp, and Madeleine Udell. Low-rank tucker approximation of a tensor from streaming data. *SIAM Journal on Mathematics of Data Science*, 2(4):1123–1150, 2020.
- [68] Yiming Sun, Yang Guo, Joel A. Tropp, and Madeleine Udell. Tensor random projection for low memory dimension reduction. *arXiv preprint arXiv:2105.00105*, 2021.
- [69] Joel A. Tropp, Alp Yurtsever, Madeleine Udell, and Volkan Cevher. Streaming low-rank matrix approximation with an application to scientific simulation. *SIAM Journal on Scientific Computing*, 41(4):A2430–A2463, 2019.
- [70] L. R. Tucker. Some mathematical notes on three-mode factor analysis. *Psychometrika*, 31:279–311, 1966.
- [71] Beata Turoňová, Florian K. M. Schur, William Wan, and John A. G. Briggs. Efficient 3d-ctf correction for cryo-electron tomography using novactf improves subtomogram averaging resolution to 3.4 Å. *Journal of Structural Biology*, 199:187 – 195, 2017.
- [72] Kutti R Vinothkumar and Richard Henderson. Single particle electron cryomicroscopy: trends, issues and future perspective. *Quarterly reviews of biophysics*, 49:e13, 2016.
- [73] Cédric Vonesch, Lanhui Wang, Yoel Shkolnisky, and Amit Singer. Fast wavelet-based single-particle reconstruction in cryo-em. In *2011 IEEE International Symposium on Biomedical Imaging: From Nano to Macro*, pages 1950–1953, 2011.
- [74] Garrett Wright, Joakim Andén, Vineet Bansal, Junchao Xia, Chris Langfield, Josh Carmicheal, Kris Sowattanangkul, Robbie Brook, Yunpeng Shi, Ayeley Heimowitz, Pragier Gabi, Itay Sason, Amit Moscovich, Yoel Shkolnisky, and Amit Singer. Computationalcryoem/aspire-python: v0.12.2. *Zenodo*, 2024.
- [75] Andy Zhang, Oscar Mickelin, Joe Kileel, Eric J. Verbeke, Nicholas F. Marshall, Marc Aurèle Gilles, and Amit Singer. Moment-based metrics for molecules computable from cryo-em images. *Biological Imaging*, page 1–22, 2024.
- [76] Wenyang Zhao, Osamu Miyashita, Miki Nakano, and Florence Tama. Structure determination using high-order spatial correlations in single-particle X-ray scattering. *IUCrJ*, 11(1):92–108, 1 2024.
- [77] Zhizhen Zhao, Yoel Shkolnisky, and Amit Singer. Fast steerable principal component analysis. *IEEE Transactions on Computational Imaging*, 2(1):1–12, 2016.
- [78] Zhizhen Zhao and Amit Singer. Fourier-bessel rotational invariant eigenimages. *Journal of the Optical Society of America. A, Optics, image science, and vision*, 30 5:871–7, 2012.
- [79] Ellen D. Zhong, Tristan Bepler, Bonnie Berger, and Joseph H. Davis. Cryodrgn: reconstruction of heterogeneous cryo-em structures using neural networks. *Nature Methods*, 18(2):176–185, 2 2021.
- [80] Ellen D. Zhong, Tristan Bepler, Joseph H. Davis, and Bonnie Berger. Reconstructing continuous distributions of 3d protein structure from cryo-em images. In *International Conference on Learning Representations*, 2019.
- [81] Gustav Zickert, Ozan Öktem, and Can Evren Yarman. Joint gaussian dictionary learning and tomographic reconstruction. *Inverse Problems*, 38(10):105010, 9 2022.